Artificial Negative Permeability Based on a Fractal Jerusalem Cross

Undergraduate Honors Thesis by

Alexander Remley Katko

In Partial Fulfillment of the Requirements for

Graduation with Distinction

The Ohio State University

Department of Electrical and Computer Engineering

Columbus Ohio

2009

(Defended May 12th 2009)

Abstract

In recent years new fabrication methods have led to electromagnetic structures not previously possible to create at sub-wavelength sizes, opening up an entirely new field of engineering: metamaterials. These sub-wavelength structures can lead to new properties not found in nature, such as a negative index of refraction, which has been demonstrated to yield a working cloaking device. This field presents a new degree of freedom to designers but there are several issues preventing the ease of design found in more established fields. One of the problems with creating metamaterial structures is presented in the analysis of such structures. With structures of sub-wavelength size analysis has been shown to be valid if the metamaterial is considered a homogeneous material, but traditional analysis methods are unable to treat these structures as such. Thus, new analysis methods have been devised. A robust method of effective material parameter retrieval is implemented in this research with several well-known structures to demonstrate its effectiveness. The well-known structures of metamaterial research, such as split-ring resonators (SRR) and complementary electric L-C (CELC) resonators, have well-documented issues such as narrowband resonant responses, high losses, and polarization sensitivity. Metamaterial designers typically deal with a structure which simulates an artificial magnetic material, as with the aforementioned SRR and CELC structures. The novelty of this field has led many, if not most, researchers to deal either entirely with SRRs or structures very similar to them. The robust analysis method implemented in this research was used to design and characterize new metamaterial

unit particles with improvements over the traditional SRRs and CELCs. Following initial design the new particles were simulated using Ansoft's industry-standard electromagnetic simulation tool, HFSS. These simulations yielded scattering parameters for the new structures, permitting the robust analysis method to extract effective material parameters. The unit particles were designed with the goals of increasing polarization independence and making multi-band structures, enabling flexibility for designers not available with existing metamaterial unit particles. Particles based on a fractal Jerusalem Cross provided the multi-band capability not found in existing structures and increased rotational independence of the structure.

Acknowledgements

I would like to thank several people for their assistance in completing this distinction project. First, I would like to thank my advisor, Professor Ronald Reano. His expertise, resources, and, most importantly, enthusiasm and love of engineering have helped steer me through this project. He has always been available when I needed a push in the right direction but he has also let me choose the directions I wished to go, even as they changed over the course of this project. He helped build my excitement for electromagnetic modeling, analysis, and design through the many months that encompassed this project. Beyond the scope of this work, his knowledge and enthusiasm have helped inspire me in pursuing a love of engineering in many directions, from optics to RF, from metamaterials to electromagnetic modeling. I am extremely grateful and in his debt for his help, guidance, and friendship throughout the course of both my research and my undergraduate studies.

I would also like to thank some of the graduate students working with Professor Reano. Galen Hoffman, Alexander Ruege, and Justin Burr have helped me in innumerable ways. From helping me get acquainted to the lab space to useful discussions about research, all three of them helped me throughout the process of conducting this research and also helped me through my coursework.

Finally, I would like to thank Professor Betty Lise Anderson for being a member of my oral defense committee. Her enthusiasm has been an inspiration in continuing through difficult sections of research and course work, and her knowledge and analysis helped immensely in building both my oral defense and the final written version of this thesis.

Table of Contents

List of Figures

Chapter 1: Introduction

1.1 Motivation for Present Work

Engineering is a field motivated by designing new devices or processes using available resources to their fullest extent. Radio frequency, or RF, engineers design using materials and devices with properties important in RF, typically defined as frequencies with an upper bound of the millimeter-wave band, at 300 GHz [1]. Recent and continuous advances in wireless technology, particularly relating to wireless internet and cellular telephone communications, have led to corresponding recent and continuous advances in RF design techniques and tools [2]. Traditional electrical design tools, like lumped element circuit building blocks, are inadequate for RF design [3]. The lead wires of capacitors and resistors, for instance, behave as inductors at RF. Traditional electrical filters, like simple RLC circuits, do not function as desired when the wavelength of the system approaches the physical circuit dimensions. When this happens, circuits and systems must be analyzed using different approaches, namely transmission line analysis or direct analysis using Maxwell's equations [4]. Transmission line analysis is an intermediate form of analysis, bridging the gap between the simplifications of lumped element analysis and the generality of Maxwell's equations. With high enough frequency, however, it becomes necessary to utilize Maxwell's equations directly.

There are numerous varieties of tools available to analyze and design circuits without frequency limitations. Very popular methods utilize full-wave analysis. There are many ways of discretizing and

manipulating Maxwell's equations for use in computer analysis, including the finite integration method (FIM), finite element method (FEM), and finite difference time domain (FDTD) method [5]. Each of these techniques has distinct advantages and disadvantages, but each also has the generality to analyze any given electromagnetic problem of interest. The methods are, however, very different from those used in, for example, SPICE analysis for lower frequency problems [6].

Just as the analysis and design methods are very different in RF design, the building blocks for design are also very different. Traditional lumped element building blocks with lead wires are not good tools for higher frequency RF design. Some building blocks, like transistors, can be used at higher frequencies, but their requirements become more and more strict for retaining their usefulness without introducing unwanted features. Moreover, a transmission line approach must generally be taken to describe the RF network. Simple bare wires radiate as antennas when comparable in size to the wavelength of interest and so other types of transmission lines are typically used. Waveguides, coaxial cables, stripline, and microstrip structures are all frequently used in different situations [4]. Microstrip and stripline structures are very attractive for several reasons. First, they are very easy to fabricate. Second, there is much flexibility in the designs, with the ability to choose a dielectric substrate and contact metal and even to vary these materials throughout a single design. Third, radiating elements (antennas) can be easily incorporated on to a structure to increase miniaturization.

As frequencies become higher and higher, circuit elements necessarily become smaller and smaller. Recent advances in circuit fabrication technology have been extended from traditional microstrip circuits to other types of designs. The ability to create structures consisting of both metals and dielectrics on a very small scale has opened up an entirely new field, metamaterial design. Naturally occurring materials can only be treated as homogeneous if any structural variations are significantly smaller than the wavelength. X-ray diffraction is possible to use for measurements in semiconductors

because the wavelength is at a comparable size to structural elements [7]. As long ago as 1948, structures at very small scales have been fabricated to mimic properties of naturally-occurring materials without using similar natural materials [8]. Early research used metals to create structures that mimicked dielectrics. It is well-known that an array of thin wires can behave like a naturally-occurring plasma [9]. More recently, it has been discovered that small-scale structures of metals and dielectrics can exhibit properties that do not occur in nature. One of the most important discoveries was that of the split-ring resonator, which behaves like a "magnetic plasma" at certain frequencies [10]. The SRR exhibits a negative effective permeability at certain frequencies, an effect that is not found in nature. The realization of this phenomenon was important due to a theoretical study published decades before [11]. In [11] it was shown theoretically that if a material could have simultaneously negative permeability and permittivity, the material would also have a negative index of refraction and would behave as a "left-handed" medium. The SRR, studied in [10], enabled the construction of a material with both negative permeability and permittivity, allowing the experimental verification of a metamaterial with a negative index of refraction in [12].

The analysis of these effective metamaterials has also required new methods to analyze networks. RF network analysis has used analytical methods to derive effective homogeneous material parameters from traditional measured quantities, such as scattering parameters [13]. The method developed in [13] by Nicolson and Ross is commonly referred to as the NRW method, for [13] and a related paper [14] by Weir. The NRW method is very effective for many traditional materials. However, it is inadequate for metamaterial analysis for reasons that will be discussed later. Thus, metamaterial research has led not only to new types of materials but new ways to analyze materials.

The recent verification of such a metamaterial has led to an explosion in research relating to a negative index of refraction. Negative index media have led to advances in areas from creating perfect

lenses [15] to cloaking devices [16]. One of the issues with current metamaterials, however, is the lack of design flexibility in constitutive particles. SRRs are still easily the most widely-used structures, although they exhibit narrow bandwidth and only a single region of interest since they operate as resonant structures. The array of thin, straight wires is also the most widely-used structures to obtain negative permittivity. Variants of these are also commonly used, including capacitively-loaded strips (CLS, [17]) and complementary electric L-C resonators (CELC, [18]). All of these structures have limitations, however, including polarization dependence and the noted narrow bandwidth. Some recent research has focused on creating negative permeability structures with multiple bands by combining SRRs in interesting ways [e.g. 19]. Even so, there exists a need for new particles to create metamaterials. The focus here will be on structures exhibiting negative permeability. Current structures like SRRs are studied and new constitutive structures based loosely on SRRs are created.

1.2 Outline of This Thesis

This report will explore current issues relating to metamaterials. Chapter two will analyze and implement the finite difference time domain simulation method to study issues regarding electromagnetic simulations. Chapter three will examine negative index metamaterials and analysis methods, including the implementation of a robust analysis method that overcomes problems present in more venerable methods. Chapter four will analyze current metamaterial constitutive structures using the tools developed in the previous chapters and will include the development of novel structures.

Chapter 2: Finite Difference Time Domain Modeling

2.1 Explanation of Maxwell's Equations and Notation

The solution of Maxwell's equations, even considering many simplifying assumptions, is generally not possible in closed form. Thus, practical problems make use of numerical modeling techniques. As mentioned above, there are numerous ways of modeling complex electromagnetic systems. Reference [5] contains descriptions and implementations of several useful methods. An exemplary modeling method was chosen and analyzed to gain understanding of numerical modeling of complex electromagnetic structures, such as those with negative effective index. The finite difference time domain (FDTD) method was chosen for several reasons. First, the FDTD method is conceptually easy to understand and implement. It is directly derived from the differential forms of Maxwell's equations. The FDTD method is also both venerable and very powerful. As a time-domain method, it is well-equipped to deal with designs where a wide bandwidth of analysis is desired. Commercial implementations of the method are commonly found and used for wideband designs. RSOFT FullWAVE is an exemplary commercial analysis package utilizing the FDTD method. The derivation of the FDTD method will be considered here and implemented using MATLAB, a popular and widely-available general purpose scientific computing package.

All electromagnetic simulation algorithms are fundamentally derived from Maxwell's equations. The most general forms of Maxwell's equations can be presented in either differential or integral forms

[19]. The differential forms will be considered here and are presented below, with physical meanings of the symbols listed in Table 2.1.1.

$$\nabla \times \vec{H} = \vec{J}_{ic} + \frac{\partial \vec{D}}{\partial t} \quad 2.1.1$$

$$\nabla \times \vec{E} = -\vec{M}_i + \frac{\partial \vec{B}}{\partial t} \quad 2.1.2$$

$$\nabla \cdot \vec{D} = \rho_{ev} \quad 2.1.3$$

$$\nabla \cdot \vec{B} = \rho_{mv} \quad 2.1.4$$

Table 2.1.1: List of Parameters in Maxwell's Equations

Symbol	Description
$\vec{H}$	Magnetic Field Intensity
$\vec{E}$	Electric Field Intensity
$\vec{D}$	Electric Flux Density
$\vec{B}$	Magnetic Flux Density
$\vec{J}_{ic}$	Source and Conduction Electric Current Density
$\vec{M}_i$	Source Magnetic Current Density
ρ_{ev}	Electric Charge Density
ρ_{mv}	Magnetic Charge Density

Two of the parameters listed in eqns. 2.1.1-2.1.4 are non-physical and simply useful for analysis ($\vec{M}_i$ and ρ_{mv}). Maxwell's equations can be written succinctly and are relatively simple, but they are not easy to solve. There are several auxiliary equations which relate the field intensities to flux densities, known as the constitutive equations. They are given below.

$$\vec{D} = \bar{\bar{\varepsilon}} \cdot \vec{E} \quad 2.1.5$$

$$\vec{B} = \bar{\bar{\mu}} \cdot \vec{H} \quad 2.1.6$$

The parameters ε and μ are known as the electric permittivity and magnetic permeability, respectively. In general they may both be functions of direction, in which case they can be represented by 3x3 matrices. If they are equal in all directions within a material, the material is known as isotropic. If the permittivity and permeability tensors are equal at all points with a material, the material is known as homogeneous. In most real materials both permittivity and permeability are functions of frequency and these are known as dispersive materials. In this case, the operation in eqns 2.1.5 and 2.1.6 becomes convolution in the time domain. Another equation is also used to relate the current density to the field intensities, shown below.

$$\vec{J} = \bar{\bar{\sigma}} \cdot \vec{E} \qquad 2.1.7$$

The parameter σ is the electric conductivity. An analogous parameter σ_m may also be defined as the magnetic conductivity, although only the electric conductivity is physically meaningful. Equation 2.1.7 is known as Ohm's Law in point form.

Solutions of Maxwell's equations can take several forms. The general form, and that considered throughout this thesis, will be a time-harmonic plane wave solution. The convention used here is shown below, using the electric field intensity as an example.

$$\vec{E}(\vec{r}, t) = \vec{E}_0 e^{j(\omega t - \vec{k} \cdot \vec{r})} \qquad 2.1.8$$

Strictly speaking the field is actually the real part of the right side of 2.1.7, but this convention is commonly used throughout the literature and will be used here. The symbol $\vec{r}$ above is the position vector and $\vec{k}$ is the wavevector. Some confusion can arise due to this notation. Namely, another convention is commonly used in physics literature, shown below, where the physical description is the same.

$$\vec{E}(\vec{r}, t) = \vec{E}_0 e^{i(\vec{k} \cdot \vec{r} - \omega t)} \qquad 2.1.9$$

This thesis will use the first convention and will note any differences in formulation in the literature as they arise. The formulation assumes a time-harmonic field dependence, which is standard. With this understanding, field quantities will typically be written with the $e^{j\omega t}$ factor omitted for space.

2.2 Derivation of Continuous-Time Difference Equations

As written in section 2.1, Maxwell's equations are too general for simple application in a numerical model and some assumptions need to be made to simplify analysis and formulation. The equations will be formulated assuming homogeneous, isotropic media. The validity of this approach for normal materials depends on the individual medium of concern. General dielectric materials are usually well-represented as homogeneous, isotropic media in most analysis. The validity of this assumption for metamaterials will be addressed in the following chapter. Another assumption made here initially will be that of a source-free region of interest. Mathematically that means that the charge distributions (ρ_{ev} and ρ_{mv}) and current densities ($\vec{J}_{ic}$ and $\vec{M}_i$) will be identically zero. Also initially, the material will be considered to be non-dispersive and lossless, equating to the conductivities (σ and σ_m) being identically zero, and the parameters ε and μ being constant with frequency. These simplifications do not truly describe any physical medium, but they are useful for an initial modeling formulation.

These assumptions and simplifications can be shown to yield the following equations directly from Maxwell's equations and the constitutive equations.

$$\frac{\partial \vec{E}}{\partial t} = \frac{1}{\varepsilon_r \varepsilon_0} \nabla \times \vec{H} \qquad 2.2.1$$

$$\frac{\partial \vec{H}}{\partial t} = -\frac{1}{\mu_0} \nabla \times \vec{E} \qquad 2.2.2$$

Here the assumption has also been made that the material is nonmagnetic. The following formulation will follow that developed and presented in [20]. Gaussian (cgs) units will be utilized in this formulation

since typical field values of E and H may be orders of magnitude apart, which provides a satisfying duality when implemented. This is accomplished by normalizing *E* as shown below.

$$\tilde{E} = \sqrt{\frac{\varepsilon_0}{\mu_0}}\vec{E} \qquad 2.2.3$$

This chapter will deal only with one-dimensional simulations for simplicity in implementation. The formulation of equations is simple in two dimensions and somewhat more complex in three. Further excellent discussions and many more in-depth considerations of the FDTD method can be found in [21]. In the media discussed, an appropriate mode of propagation is the transverse-electromagnetic (TEM) mode, which will be implemented here. The propagation direction will be *z*, the electric field will be polarized along *x*, and the magnetic field will be polarized along *y*. Utilizing this formulation, eqns. 2.2.1 and 2.2.2 can be simplified into the below forms.

$$\frac{\partial \tilde{E}_x}{\partial t} = \frac{1}{\varepsilon_r\sqrt{\varepsilon_0\mu_0}}\frac{\partial H_y}{\partial z} \qquad 2.2.4$$

$$\frac{\partial H_y}{\partial t} = -\frac{1}{\sqrt{\varepsilon_0\mu_0}}\frac{\partial \tilde{E}_x}{\partial z} \qquad 2.2.4$$

These equations can be easily transformed into discrete-time versions for implementation on a computer, as will be shown in the following section.

The preceding formulation was largely illustrative and used to examine manipulation of Maxwell's equations directly. Using similar assumptions and derivations, other useful formulations of Maxwell's equations can be developed for appropriate studies. Following [22], formulations can be made using the current densities as below.

$$\partial_t E_x = \frac{1}{\varepsilon_0}(-\partial_z H_y - J_x) \qquad 2.2.5$$

$$\partial_t J_x + \Gamma J_x = \varepsilon_0\omega_p^2 E_x \qquad 2.2.6$$

$$\partial_t H_y = \frac{1}{\mu_0}(-\partial_z E_x - K_y) \quad 2.2.7$$

$$\partial_t K_x + \Gamma K_x = \mu_0 \omega_p^2 H_y \quad 2.2.8$$

These formulations arise from considering a homogeneous lossy Lorentz medium for both the permittivity and permeability. This type of medium, with permittivity (for instance) given by a function shown below, yields the required behavior for a material with negative permittivity or permeability.

$$\varepsilon(\omega) = \varepsilon_0\left(1 - \frac{\omega_p^2}{\omega^2 + i\Gamma\omega - \Gamma^2}\right) \quad 2.2.9$$

The parameter Γ relates to losses within the material. It can be easily shown that below the plasma frequency the value of permittivity (equivalently permeability) may be negative.

2.3 Discrete-Time Implementation and Backward Wave Propagation Demonstration

The equations derived and shown previously can be easily transformed into discrete time versions. The discretization approach used when implementing these equations makes a large difference in the order of error introduced. Some different approaches and the order of error introduced by them can be found in [5]. The approach implemented here was chosen for accuracy and simplicity. For any function *f(x)*, its derivative can be approximated as shown below.

$$f'(x_0) \approx \frac{f(x_0+\Delta x) - f(x_0-\Delta x)}{2\Delta x} \quad 2.3.1$$

This approach is known as the central difference approximation, since it approximates the derivative in the center of an interval. As in [5], the order of error introduced by this approximation is (Δx^2). Typically this is very small relative to the wavelength of interest and introduces very small errors. The

remainder of this chapter will deal with discrete functions of both time and space, so some notation will be introduced. The notation used is shown below for the electric field as an example.

$$E_x^n(k) = E(n\Delta t, k\Delta x) \qquad 2.3.2$$

This notation is used primarily to save space. Considering first equations 2.2.4 and 2.2.5, the question arises of how to discretize these for easy implementation. The answer was first laid out in [23] in a seminal paper by Yee. The approach taken is a "stair-stepping" technique. Rather than find both field values at the same points in space and time, the fields are found at slightly different points. In the implementation used here, for instance, the electric field will be determined at integer points in space and integer + ½ points in time, while the converse is true for the magnetic field. This allows all field values at all points in space and time to be found using an initial value at any single point. Implementing this scheme (known as the Yee cell in three dimensions) yields discretized versions of equations 2.2.4 and 2.2.5 shown below.

$$\frac{E_x^{n+\frac{1}{2}}(k) - E_x^{n-\frac{1}{2}}(k)}{\Delta t} = -\frac{1}{\varepsilon_r\sqrt{\varepsilon_0\mu_0}}\frac{H_x^n\left(k+\frac{1}{2}\right) - H_x^n\left(k-\frac{1}{2}\right)}{\Delta z} \qquad 2.3.3$$

$$\frac{H_x^{n+1}\left(k+\frac{1}{2}\right) - H_x^n\left(k+\frac{1}{2}\right)}{\Delta t} = -\frac{1}{\sqrt{\varepsilon_0\mu_0}}\frac{E_x^{n+\frac{1}{2}}(k+1) - E_x^{n+\frac{1}{2}}(k)}{\Delta z} \qquad 2.3.4$$

As seen in equations 2.3.3 and 2.3.4, the value of *E* at a given time and position depends on the value of *E* at the same position but previous time and the current values of *H* at adjacent positions. The same is true for *H*. Thus, a leapfrog approach can be implemented rather easily. Equations 2.3.3 and 2.3.4 can be solved for the new field values in time to yield the following equations.

$$E_x^{n+\frac{1}{2}}(k) = E_x^{n-\frac{1}{2}}(k) - \frac{\Delta t}{\varepsilon_r\sqrt{\varepsilon_0\mu_0}\Delta z}\left(H_x^n\left(k+\frac{1}{2}\right) - H_x^n\left(k-\frac{1}{2}\right)\right) \qquad 2.3.5$$

$$H_x^{n+1}\left(k+\frac{1}{2}\right)=H_x^n\left(k+\frac{1}{2}\right)-\frac{\Delta t}{\sqrt{\varepsilon_0\mu_0}\Delta z}\left(E_x^{n+\frac{1}{2}}(k+1)-E_x^{n+\frac{1}{2}}(k)\right) \quad 2.3.6$$

These equations are the ones which will be implemented.

MATLAB was used to implement this algorithm. Different materials can be specified by varying the relative dielectric constant spatially, allowing simulation of an arbitrary electromagnetic source and wave propagation through any nondispersive dielectric system. There are still a few remaining questions, however. First is the choice of appropriate size of time and frequency steps. The determination is made by the physicality of the problem. In free space, a wave propagating a distance of Δz does so in time $c\Delta t$. We can choose the spatial step Δz somewhat arbitrarily depending upon the desired accuracy. Higher accuracy corresponds to a smaller step Δz but also to a larger computational domain and, hence, lower simulation performance. Extremely small step sizes also may introduce errors due to the computing system used. Very small spatial steps will correspond to very small variations in fields between cells, and at some limit there will be truncation errors. Once the spatial step size is chosen, however, we have an upper bound for the time step. This is known as the Courant condition. It is somewhat different in higher dimensions, however. In two dimensions the maximum distance radiation may be allowed to propagate per cell is not the side of a cell, but the diagonal, or $\sqrt{2}\Delta z$. The three-dimensional case is similar. The Courant condition for an *n*-dimensional problem is thus described by the following equation.

$$\Delta t \leq \frac{\Delta z}{\sqrt{n}c} \quad 2.3.7$$

For the simple implementation corresponding to this derivation, the time step is chosen such that

$$\Delta t = \frac{\Delta z}{2c} \quad 2.3.8$$

This follows the choice made in [20].

There is another important issue involving discretization of Maxwell's equations. Any discrete computer environment can only simulate a finite domain in both space and time. The temporal size of the domain is generally chosen so that any phenomena of interest can be observed, which depends on the spatial size of the domain. However, the leapfrog approach of Yee encounters problems at the spatial edges of the domain. This necessitates an appropriate boundary condition. Possible boundary conditions include a perfect electric conductor (PEC), perfect magnetic conductor (PMC), periodic boundary conditions (PBC), and others. The one appropriate for radiation in free space is the absorbing boundary condition (ABC). In higher dimensions ABCs are generally implemented as perfectly-matched layers (PMLs) and require careful design. For this one-dimensional case, however, a simpler solution is possible (and used). The ABC in one dimension is generally implemented by storing the field values of cells adjacent to the edges of the domain for an appropriate number of time steps and using them to update the field values at the edges. The number of time steps required to be stored depends on the square root of the relative dielectric constant and on the time step chosen. For this implementation, two time steps must be stored on each side. This ensures that the field will not experience spurious reflections at the edges of the computational domain.

The entire algorithm described in this chapter, including the ABCs and Courant condition, have been implemented in MATLAB. The actual code is included as Appendix A. For this example implementation the source used is a Gaussian pulse in the middle of the spatial domain. After 100 time steps, the pulse has propagated in both directions, as expected in free space. The simulation after 100 time steps is shown in figure 2.3.1 below.

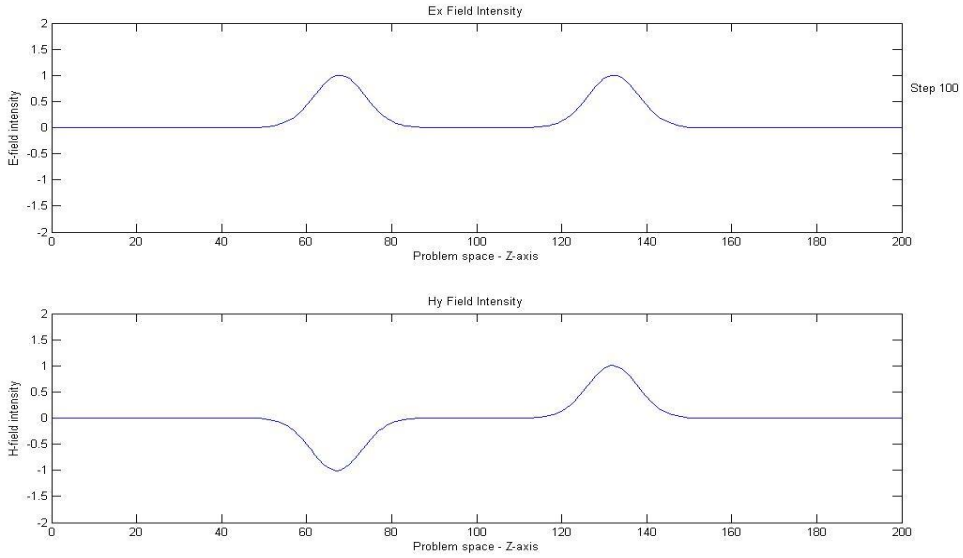

Figure 2.3.1: Simple FDTD Simulation After 100 Time Steps

As seen in the figure, the simulation works as expected for propagation in free space. There is a dielectric interface at *z*=150 of size 30, where the relative dielectric was given by $\varepsilon_r = 4$. The pulse impinging on the dielectric interface from the same simulation is shown below in figure 2.3.2.

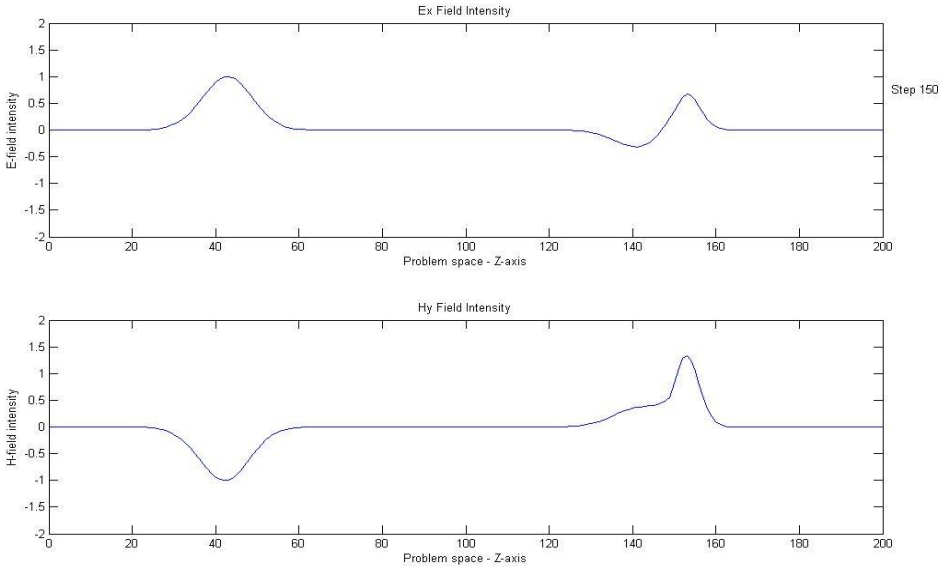

Figure 2.3.2: Simple FDTD Simulation After 150 Time Steps

This simulation clearly shows the original pulse continuing to propagate leftward. It also shows a partial transmission and partial reflection at the dielectric interface in both *E* and *H*. With an interface as such we expect a field reflection coefficient

$$\Gamma = \frac{\sqrt{\varepsilon_r}-1}{\sqrt{\varepsilon_r}+1} = \frac{1}{3} \qquad 2.3.9$$

and this is indeed what is shown with the electric field. In order to illustrate the effectiveness of the ABCs, another snapshot was taken of the same simulation after 300 time steps and is shown in figure 2.3.3 below.

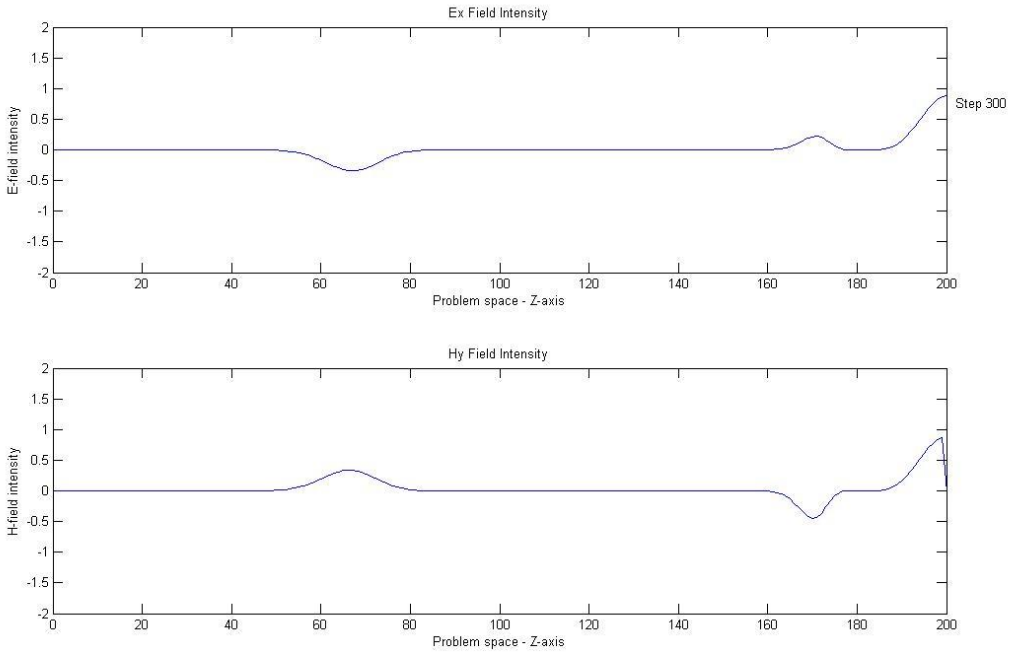

Figure 2.3.3: Simple FDTD Simulation After 300 Time Steps

The original pulse propagating leftward has been absorbed by the ABC and the left pulse is due to reflection at the dielectric interface. The original pulse is being absorbed in this figure on the right. The middle, smaller pulse is due to a reflection at the other side of the dielectric. Everything shown in the series of figures illustrated the simulation and its functionality, including a source excitation, reflection

and transmission at multiple dielectric interfaces, and absorbing boundary conditions on both sides of the domain.

The work shown in this chapter has developed an FDTD implementation in one dimension and shown its implementation for a simple medium. As described in the previous section, codes can be implemented using other field equations when appropriate. Another set of code was developed and implemented based on equations 2.2.5-2.2.8. This implementation utilized equations including magnetic and electric current densities and is efficient for Lorentz media. Reference [22] includes some sample implementations of this type of medium in both one and two dimensions. The leapfrog approach is used here as well, but there are four primary quantities that must be calculated at every step in space and time. The implemented code is included as Appendix B. The code utilizes parameters used in [22] to create a material approximately matched to free space in magnitude of refractive index and impedance. Using the Lorentz model given earlier, the script in Appendix B calculates the material parameters as shown in table 2.3.1.

Table 2.3.1: Calculated Material Parameters

Parameter	Value	Free Space Value
Permittivity ε	-8.8443e-012 +9.3892e-015i	8.854e-012
Permeability μ	-1.2553e-006 +1.3326e-009i	1.2566e-06
Impedance Z	376.73 -3.1032e-017i	376.7343

As shown in Table 2.3.1, both permittivity and permeability are dispersive by virtue of being complex. This is important for reasons that will be discussed in the following chapter. Also note that the real parts of all listed parameters are very close to free-space values. This was done to reduce any impact of

reflections at the material interfaces and to isolate the effects of a material with NRI. The index and impedance profiles are shown below in figure 2.3.4.

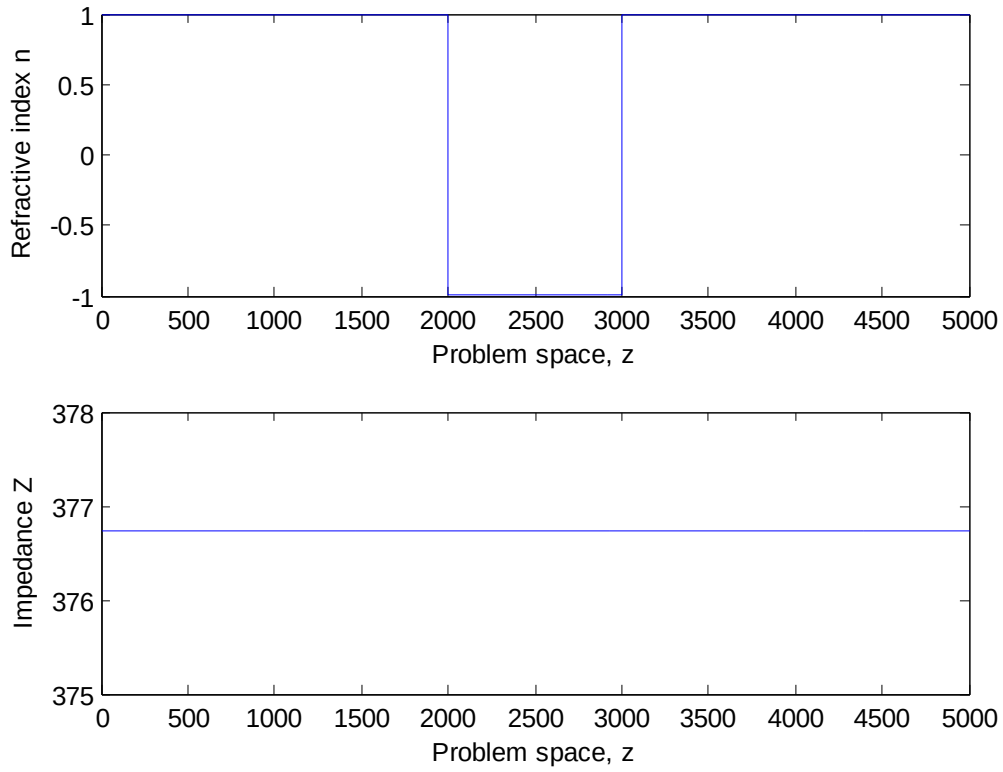

Figure 2.3.4: Index and Impedance Profiles for NRI Simulation

The source used is a continuous-wave (CW) electric field source located at *z*=500. The script calculates the field quantities as described previously. It also calculates the instantaneous Poynting vector at all points in time and space, which is simple to find when the fields are both known as given by $\vec{P} = \vec{E} \times \vec{H}$. One aspect of the FDTD method not previously mentioned is that it explicitly includes transients and is not only a steady-state simulation algorithm. Once the simulation has gone through 44,000 time steps and is approximately at steady-state, the instantaneous Poynting vector at every point in the domain is time-averaged across 900 time steps. This result is shown below in figure 2.3.5.

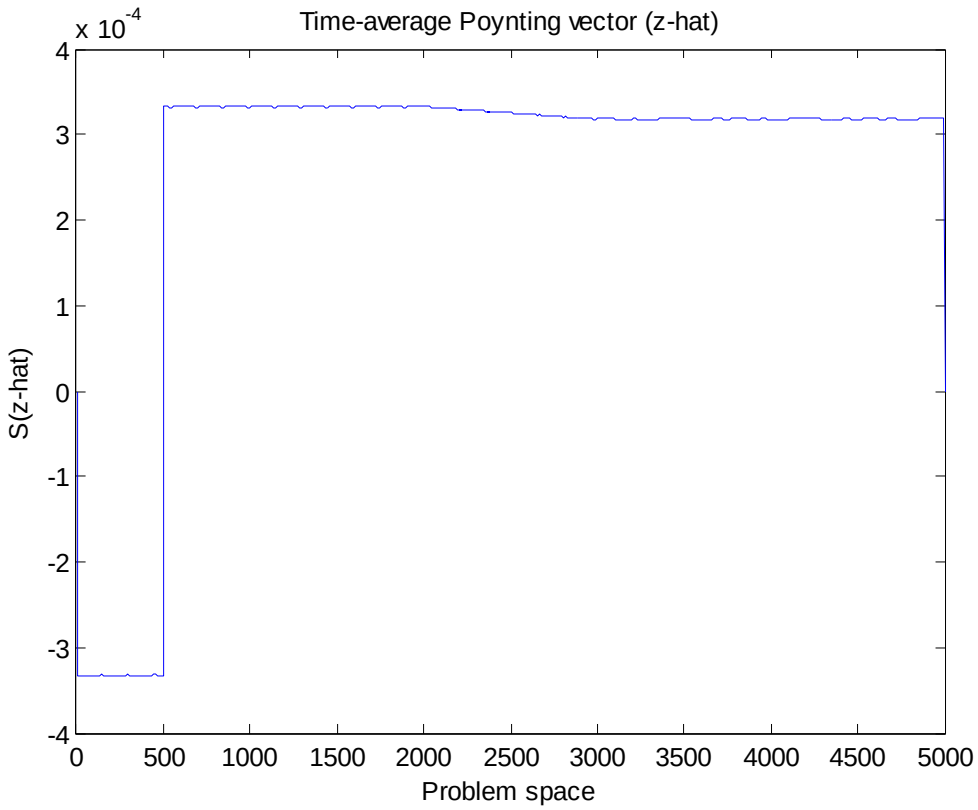

Figure 2.3.5: Time-Averaged Poynting Vector in Steady-State Simulation

Since the Poynting vector is emphatically a vector, it conveys more information than immediately apparent. The region with a negative value signifies that power flows in the negative-*z* direction for this region. This is exactly what is expected, as the source is located in free space to the right of the region. Similarly, the sign of the remainder of the domain indicates that power is directed along the positive-*z* direction. This is important as it shows the causality of the NRI region, as will be discussed in the following chapter. The time-averaged Poynting vector is also nearly constant through both free space and the NRI region. There are some variations in the domain due to the fact that transients have not entirely died out after 44,000 time steps. There is also a small mismatch between the NRI region and free space, and the NRI region has small but finite imaginary parts of refractive index and impedance, leading to some (very small) dispersive losses.

Due to the nature of the FDTD method, it is very easy to watch a simulation and observe backward-wave propagation. It is, however, somewhat more difficult to illustrate in print, as in this thesis. Figure 2.3.6 below shows the electric and magnetic fields and instantaneous Poynting vector at the end of the simulation.

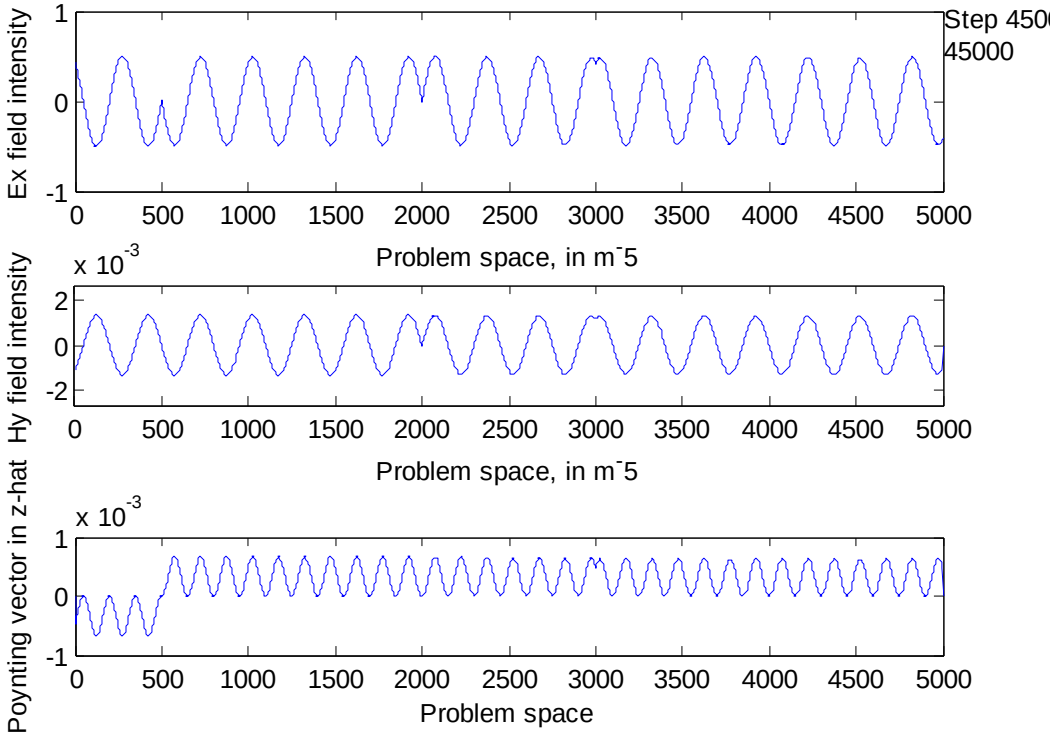

Figure 2.3.6: Negative Index Simulation After 45000 Steps

As observed in this figure, the region of NRI is from z=2000 to z=3000. To preserve causality, the front of the wave crosses the entire NRI region before backward propagation is observed, corresponding to the causality of information. As shown in figure 2.3.7 below, the wave has reached the NRI region but backward propagation is not occurring in the steady-state after 2000 time steps.

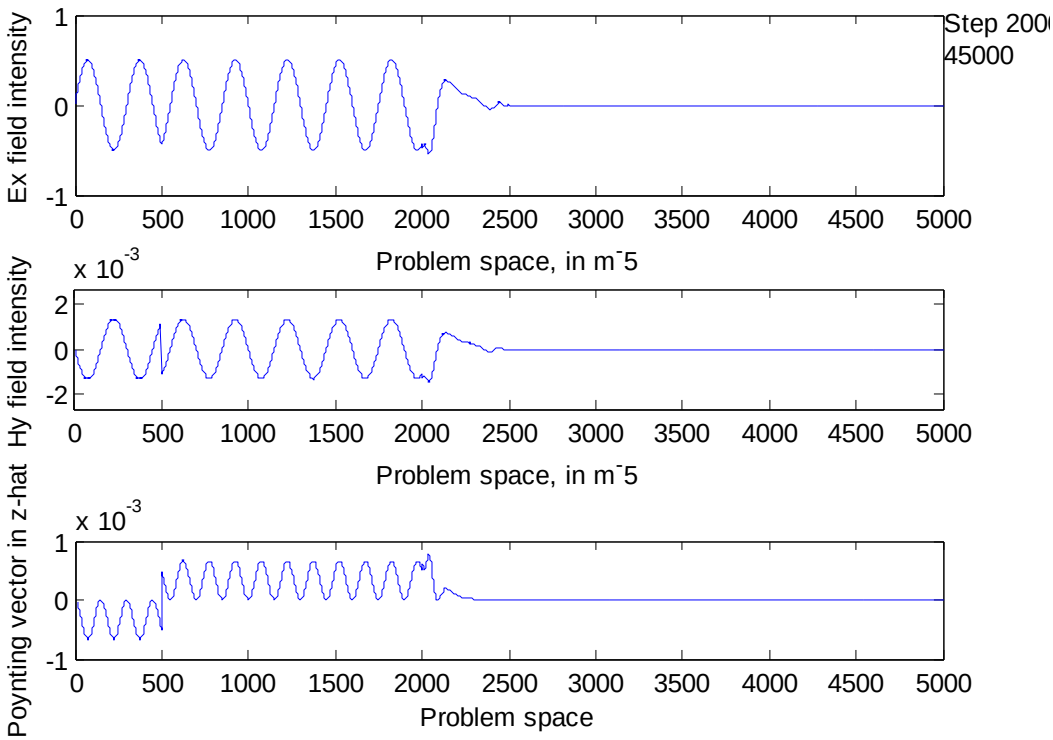

Figure 2.3.7: Negative Index Simulation After 2000 Steps

After a further 1000 time steps the front of the wave has reached the other side of the NRI region and passed through, shown in figure 2.3.8 below.

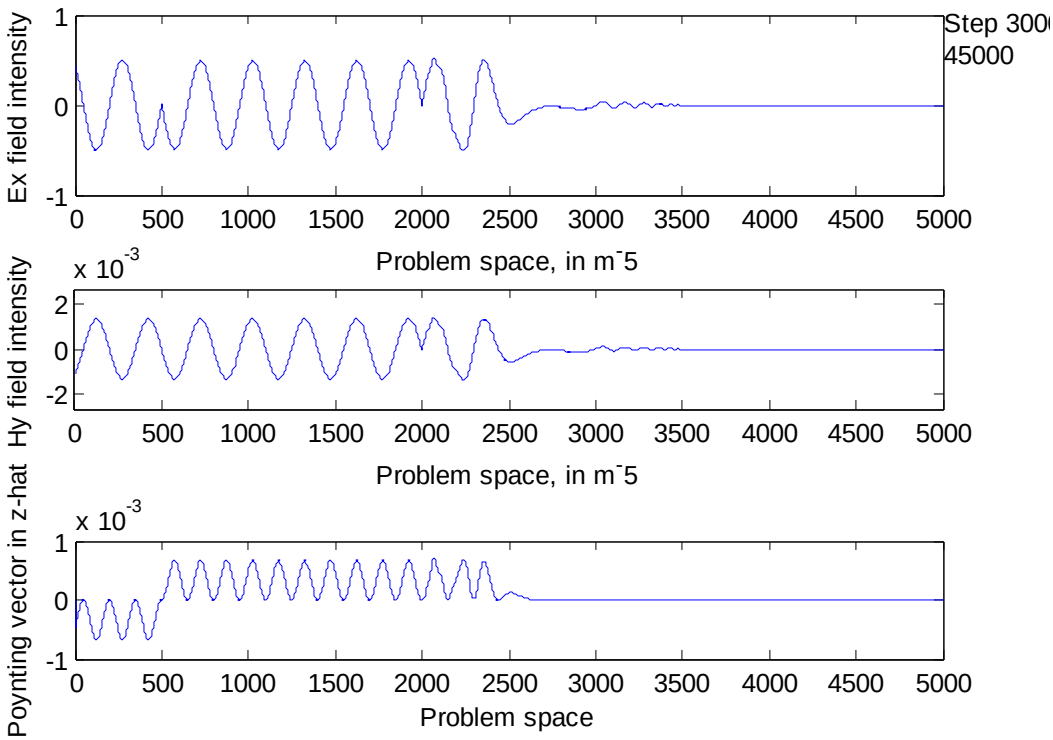

Figure 2.3.8: Negative Index Simulation After 3000 Steps

Backward propagation has started in the NRI region at this point but has not reached steady-state. In order to illustrate backward propagation in the NRI region without including multimedia files, two snapshots with a short time separating them will be presented which clearly show backward propagation. These are presented in figure 2.3.9 and 2.3.10.

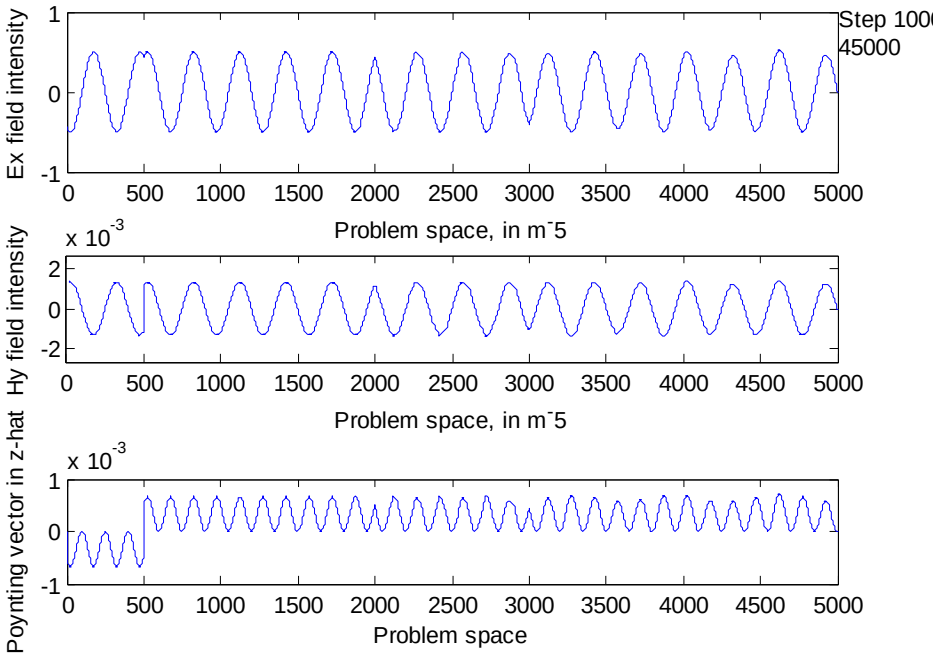

Figure 2.3.9: Negative Index Simulation After 10000 Steps

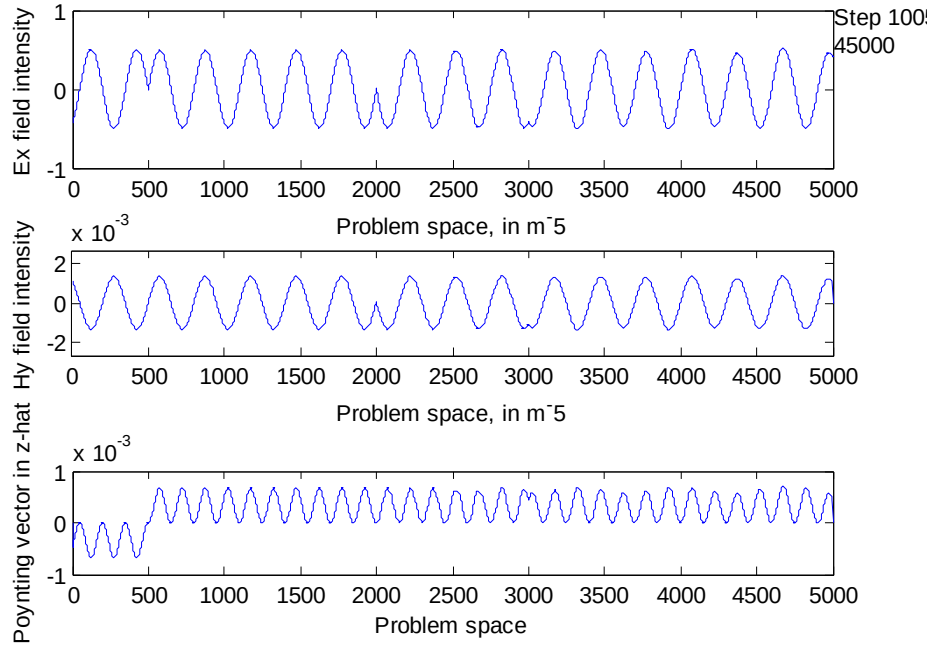

Figure 2.3.10: Negative Index Simulation After 10050 Steps

Careful examination of individual peaks between the two figures shows clearly that the wave propagates leftward between z=2000 and z=3000 and propagates rightward elsewhere. This simulation verifies many of the important properties of NRI metamaterials. First, causality is preserved. While the phase velocity of the wave may be reversed with a change in sign of refractive index, the Poynting vector shows that the direction of power flow (and thus information) remains the same. Second, backward wave propagation is demonstrated in a homogeneous material.

The FDTD method was analyzed and successfully implemented for multiple cases. First, a simple example was carried through all steps and demonstrated to yield expected analytical results, validating the method and its implementation here. Second, a more complex form of equations was implemented and tested. The results showed that for a given formulation of the FDTD method using well-known (Lorentz) material models, negative refractive index and backward wave propagation are possible. Causality and positive power flow were preserved, necessary aspects of a physical system.

The FDTD method is widely used and powerful. However, an FEM-based commercial software was used for more complicated studies in the following chapters. The time and effort required to implement a fully flexible three-dimensional FDTD simulator was deemed too much for the time constraints of this project, so commercially-available, flexible software was used. Nonetheless, the analysis of the FDTD method and implementation provided valuable experience with electromagnetic simulation and an understanding of issues involved with electromagnetic modeling. The following chapter will consider analysis of negative index materials and metamaterials in particular, including issues not found in the analysis of homogeneous materials.

Chapter 3: Negative Index Analysis

3.1 Negative Index Review

As shown in [11], a material with negative permittivity and permeability will exhibit a negative index of refraction. Chapter one discussed the earliest dates of constructing materials with negative permittivity and permeability, and some analysis shows that the SRR and negative permeability came decades after the wire array and negative permittivity. The difficulty in creating a negative index metamaterial typically comes from difficulty in creating a negative permeability structure. Reference [11] discussed many of the issues with a negative index, hereafter denoted NRI. One of the most common early questions concerning NRI metamaterials involved causality. It was shown in [24] that NRI metamaterials can exist causally if and only if they are dispersive materials. This was also examined in [11], where it was shown that positive energy is maintained only when the derivatives of μ and ε with respect to frequency are positive. This is not a practical issue, as all materials are dispersive to some extent. However, it must always be considered when simulating and analyzing metamaterials.

Some of the fundamental physical properties and consequences of a negative index of refraction will be discussed here. One of the most unnatural properties of NRI metamaterials is that the direction of refraction is reversed. This is easily seen by using Snell's Law. Consider two materials with identical magnitudes of refractive index; the only difference between the two is that one has a negative index. Snell's Law is illustrated in both cases in figures 3.1.1 and 3.1.2 below, with the reflected ray omitted.

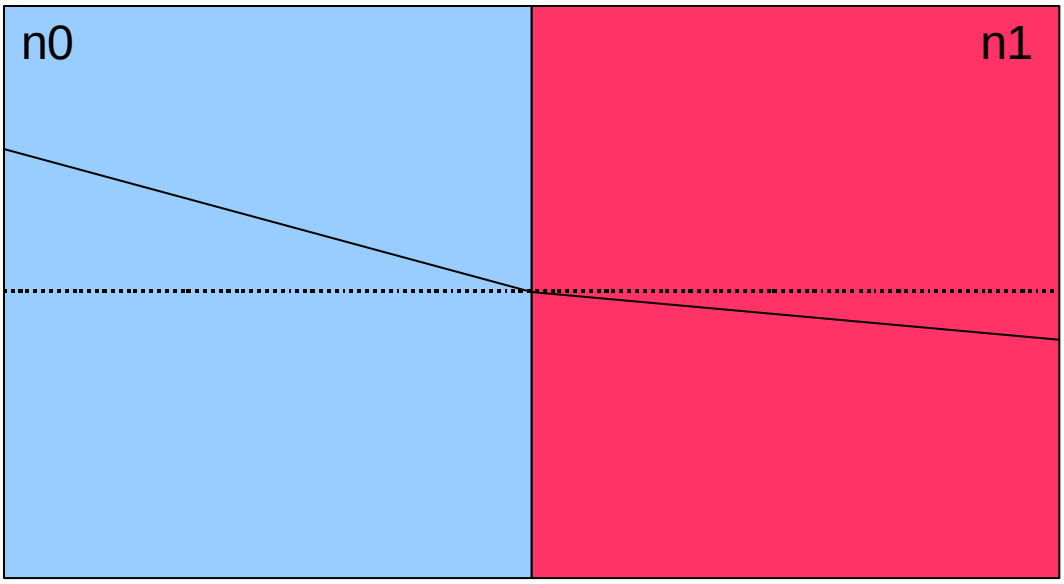

Figure 3.1.1: Refraction in Positive Refractive Index Medium

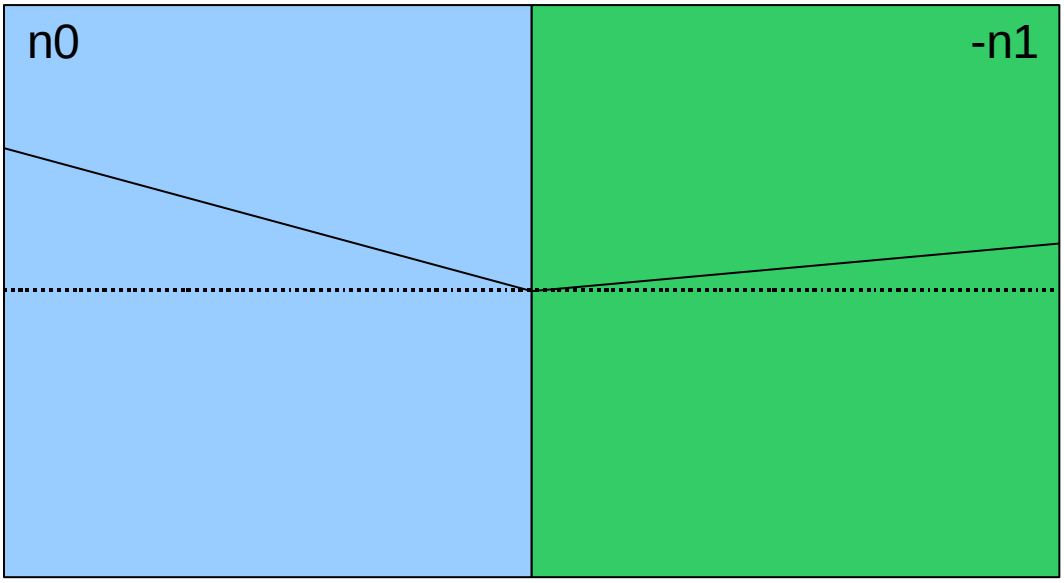

Figure 3.1.2: Refraction in Negative Refractive Index Medium

These illustrate that radiation in an NRI medium refracts to the opposite side of the normal when compared to a positive index medium [11]. The consequences and, indeed, existence of this phenomenon have been debated for years. It is now generally accepted that negative refraction exists, particularly due to numerous examples of experimental verification, beginning with [12]. One of the

earliest consequences of an NRI metamaterial was the theoretical derivation of a perfect lens in [15]. Wave propagation within NRI metamaterials has also been extensively studied. As shown analytically first in [11], the direction of the Poynting Vector and, thus, power flow is identical in both positive and negative index media. However, the phase velocity is antiparallel in the two cases, as demonstrated in chapter two. This has challenged interpretation in terms of traditional quantities like group velocity. A discussion of this can be found in chapter ten of [25]. These questions have been largely resolved, but there still exists some disagreed about interpretation of results, including, for instance, a panel discussion at the International Microwave Symposium 2009, still upcoming at the time of this publication. Debate still exists among the electromagnetics community regarding the accuracy of characterizations used for metamaterials. Experimental verification has led to wide acceptance of the phenomena discussed here, but the characterization of a metamaterial as having a negative effective index is still debated. These questions will not be addressed in this thesis.

Another very intriguing and much-analyzed consequence of the ability to engineer permittivity, permeability, and refractive index is the possibility of creating a cloaking device. The first demonstration of an entirely passive cloaking device using metamaterials was presented in [16]. This was derived based on the principles of transformation optics [26], which can also be used in other applications such as those involving conformal antenna arrays [27]. The use of transformation optics requires the ability to design metamaterials with a given permeability and permittivity which are generally inhomogeneous and anisotropic.

There are two general approaches to analyzing and designing metamaterials. The first, which will not be considered here, is the transmission line approach. As implemented in, for instance, [25], negative permeability and permittivity in a one- or two-dimensional case can be considered as a left-handed (LH) transmission line. Traditional right-handed (RH) transmission lines are represented by a

per-unit series inductance and per-unit shunt capacitance [28]. Replacing these by per-unit series capacitors and per-unit shunt inductors, as in [25], yields a LH transmission line which supports backward propagation and negative refraction (when extended to two dimensions). This analysis and design approach has led to applications such as [29] microstrip antennas with modes that are either LH or RH, leading to new radiation modes.

The second general approach is the effective-medium approach, which will be utilized here. In this approach metamaterials are treated as effectively homogeneous. This approach lends itself well to very high frequency designs and analysis and especially to volumetric design and analysis and is the approach typically used for, as in references previously mentioned, cloaking devices and perfect lenses. This approach will be discussed further in the following section.

3.2 Traditional Effective Material Analysis

Traditional effective material analysis is shown in, for example, [13] and [14] and is denoted as the NRW (Nicolson-Ross and Weir) approach. Given an arbitrary homogeneous material, two independent parameters are needed to describe it fully. The most common pairs of parameters are permeability (μ) and permittivity (ε) or refractive index (n) and material impedance (Z). They are related by the equations below.

$$\varepsilon = \frac{n}{Z} \qquad 3.2.1$$

$$\mu = nZ \qquad 3.2.2$$

An arbitrary material does not have an impedance or index that is easy to determine by measurement, however. Microwave and RF network analysis typically describes a network by a set of independent parameters, using n-port analysis [4]. Numerous approaches are used, including descriptions by the ABCD matrix, admittance matrix, and impedance matrix. The most common,

however, is the scattering (S) matrix [4]. This approach measures wave amplitudes and phases between ports in a network, yielding a matrix such as the one given below which relates incoming and outgoing waves.

$$S = \begin{bmatrix} S_{11} & S_{12} \\ S_{21} & S_{22} \end{bmatrix}$$

The measurement of S parameters is among the easiest measurement techniques at RF, typically done using a vector network analyzer. Passive networks or structures are generally symmetric, that is, $S_{ij} = S_{ji}$ for all *i, j*. When dealing with symmetric networks, then, we generally only consider S_{11} and S_{21} for a two-port network. Since all structures analyzed hereafter will be symmetric (or approximately so), this is the approach taken here.

For a one-dimensional homogeneous material of length *d*, the S parameters of the material may be determined analytically as given below.

$$S_{11} = \frac{\Gamma(1-z^2)}{1-\Gamma^2 z^2} \qquad 3.2.3$$

$$S_{21} = \frac{z(1-\Gamma^2)}{1-\Gamma^2 z^2} \qquad 3.2.4$$

Here Γ is the material reflection coefficient and *z* is a transmission coefficient between faces $z = e^{-jkd}$ with *k* denoting the wavenumber in the material. The transmission coefficient *z* can also be written as $e^{-j k_0 n d}$ where k_0 is the wavenumber in vacuum. Recalling that the reflection coefficient Γ is related to the relative material impedance by the equation

$$\Gamma = \frac{Z-1}{Z+1} \qquad 3.2.5$$

equations 3.2.3 and 3.2.4 can be inverted to find the impedance *Z* and index *n* in terms of the S parameters or, equivalently, to yield the permeability and permittivity in terms of the S parameters. The

results for permeability and permittivity can be found in reference [13], for instance. The approach considered here will determine *Z* and *n* and then use these intermediate results to calculate permeability and permittivity. Inverting equations 3.2.3 and 3.2.4 yield two equations for *Z* and *n*. The first is given below.

$$Z = \pm\sqrt{\frac{(1+S_{11})^2 - S_{21}^2}{(1-S_{11})^2 - S_{21}^2}} \qquad 3.2.6$$

Note that this is the impedance *Z* and not the transmission term *z*. The ambiguity in sign choice in this equation can be solved based on knowledge of the material in question. If the material is passive, it must have a real part of *Z* that is positive. This can be used to find the correct branch of the square root and is generally not a problem with homogeneous materials like dielectrics.

Using this result, it can also be shown that the transmission term (which contains *n*) is given by the equation below.

$$e^{-jn\,k_0 d} = \frac{S_{21}}{1 - S_{11}\frac{Z-1}{Z+1}} \qquad 3.2.7$$

This yields an equation to solve for *n* explicitly, shown below.

$$n = -\frac{1}{k_0 d}\ln\left(\frac{S_{21}}{1 - S_{11}\frac{Z-1}{Z+1}}\right) \qquad 3.2.8$$

These equations are relatively simple for determining the material parameters of a homogeneous material and have been around for decades, indeed reference [13] was published in 1970. Once one of the pairs of parameters are determined, the other pair can be easily found through equations 3.2.1 and 3.2.2 and simple algebraic manipulation.

S parameters for a given structure or network can be found experimentally or through simulation. As mentioned previously, S parameters are typically measured experimentally through the

use of a vector network analyzer. If the transmission medium is not part of a traditional transmission line like a coaxial cable, measurement horn antennas with known characteristics are typically used in conjunction with a vector network analyzer. Simulations typically calculate S parameters, whether the simulator uses an FDTD algorithm as implemented in chapter two of this thesis or another algorithm like the FEM. Due to time constraints, structures were not fabricated for this thesis. Rather, structures were simulated rigorously using Ansoft's HFSS commercial FEM software. Use of this permitted accurate and repeatable S parameter calculations as well as structurally interior field calculations. After obtaining simulation data the data was imported into MATLAB, a popular scientific computing package that is commonly used. Analysis algorithms were implemented in MATLAB. For reasons discussed in the following section, however, metamaterial analysis requires a different algorithm to retrieve effective material parameters than that traditionally used to analyze homogeneous materials.

3.3 Improved and Robust Algorithms for Analysis

Metamaterials present some unique difficulties for traditional materials analysis. Traditional analysis focuses on naturally homogeneous materials. Materials can only be considered homogeneous if any electromagnetically-important structures are significantly smaller than the wavelength [30]. The material retrieval techniques presented in the previous section have difficulties in some cases. Metamaterials with resonances and ones with either S_{11} or S_{21} close to zero can present difficulties to the retrieval process. The impedance determination of equation 3.2.6 can be made unambiguously, generally. As mentioned previously, the requirement for a passive material (or metamaterial) is that the real part of the impedance is positive. The choice of sign in equation 3.2.6 is made so that this is reinforced. Since there is only one branching problem in equation 3.2.6, determining the sign of the square root determines the real and imaginary parts of the impedance unambiguously. The only problem inherent in this approach is that numerical simulations, when giving results close to zero, may

introduce small numerical errors that could even cause a change in sign. A solution was proposed for analysis problems that encounter these errors in [31]. This solution analyzes the impedance *Z* and refractive index *n* in conjunction. Rather than determine the branch for the real part of *Z* positive, a small but finite number is used for the branch determination. All cases analyzed in this thesis did not encounter this problem, so this method is not fully used.

The problem truly arises when considering the refractive index. The impedance is determined first and then the following equation is used (reprinted for convenience from equation 3.2.8 earlier).

$$n = -\frac{1}{k_0 d}\ln\left(\frac{S_{21}}{1-S_{11}\frac{Z-1}{Z+1}}\right) \qquad 3.3.1$$

The imaginary part of *n* can be enforced and determined unambiguously when dealing with solely passive media. Depending on the notation used, the imaginary part of the index is determined unambiguously. Unfortunately there are differences in standard notation when writing the index which lead to ambiguities in sign choice. Physically, recognizing the phase term as

$$e^{-jk_0 z(n)} = e^{-jk_0 z(n' + jn'')} \qquad 3.3.2$$

shows that for the phase term to decay with increasing *z*, leads to the determination that *n''* must be less than zero. Sometimes the index is also written as $n = n' - jn''$, in which case the opposite is true. Once the sign convention is determined, however, the imaginary part of the index is determined unambiguously. Physically the requirement is that the imaginary part of the index leads to a decrease in amplitude with propagation.

Of the two independent parameters *Z* and *n*, then, three of the four necessary parts are unambiguous for a passive medium. The remainder is the real part of *n*, and it cannot easily be determined unambiguously. This arises due to the logarithm function in equation 3.3.1. The real part of

the logarithm can only be determined to within a multiple of 2π due to taking a logarithm of a complex number. Therefore, the real part of *n* is given by

$$n' \propto \left[\ln\left(e^{-j\,k_0 nd}\right)\right]'' + 2m\pi \qquad 3.3.3$$

where m is any integer. This is true for any material, but in homogeneous and naturally-occurring materials the branches due to this ambiguity are very far apart and only one solution is physically reasonable. Even so, traditional material analysis utilizes multiple samples of the same material with different thicknesses and determines the actual index by matching the branches. The effective parameter retrieval is also generally most useful and stable when the thickness of the material sample is small, in both natural material and metamaterial analysis. Without utilizing this approach, there is a certain arbitrariness to determining effective material parameters due to the branching of the logarithm.

Reference [31] presented perhaps the most effective method to determine material parameters. Several issues with effective material analysis were solved and will be discussed here. The first is with the effective size of the metamaterial sample. An optimization algorithm was used in [31] to determine the effective length of a metamaterial slab. It was found that for a one-dimensional sample, the effective length is approximately the true length of the unit cell. The metamaterial samples considered here are effectively one-dimensional, so the effective length will be taken as the actual length of the sample.

The main problem with metamaterial analysis is, as mentioned previously, choosing the correct branch of the real part of the refractive index. Generally there are only a few branches which could possibly be physically reasonable, but this is not always enough to correctly select the branch. One way to select the correct branch is presented in [31] and enforces mathematical continuity of the index. This method is rigorous and has been shown to be successful: it uses a Taylor series approximation to help

choose the correct branch at all points. However, it can encounter problems in the resonant bands so important to metamaterials. Another method for choosing the correct branch enforces continuity and utilizes multiple thicknesses of the metamaterial. With multiple thicknesses, the index branches will converge to only one true branch. Even so, continuity must be enforced with this branch. A sample metamaterial graph of index versus frequency is shown below in figure 3.3.1 to illustrate the problem.

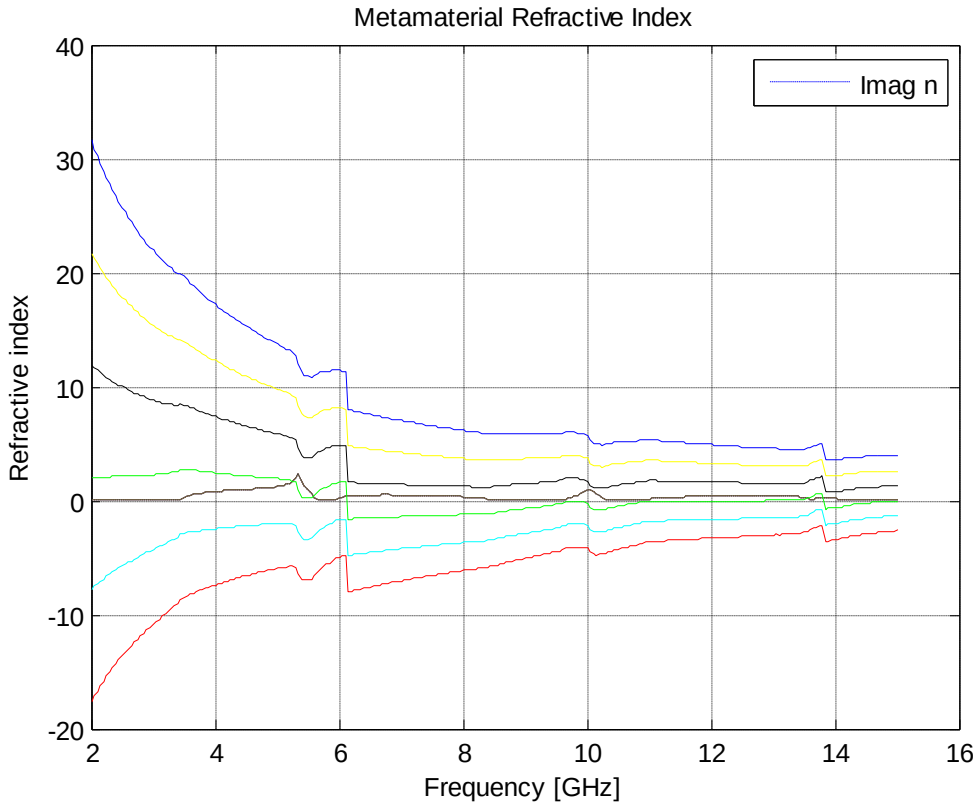

Figure 3.3.1: Branches of Metamaterial Refractive Index

The different colors of solid lines represent different branches of the logarithm. As can be seen in the figure, the branches can be very close together and it is difficult to determine the correct one. Moreover, enforcing continuity requires selecting different branches at different frequency ranges. Simulation of another thickness of the same metamaterial structure, however, enables the choice of the correct branches and yields the continuous function shown in figure 3.3.2 below.

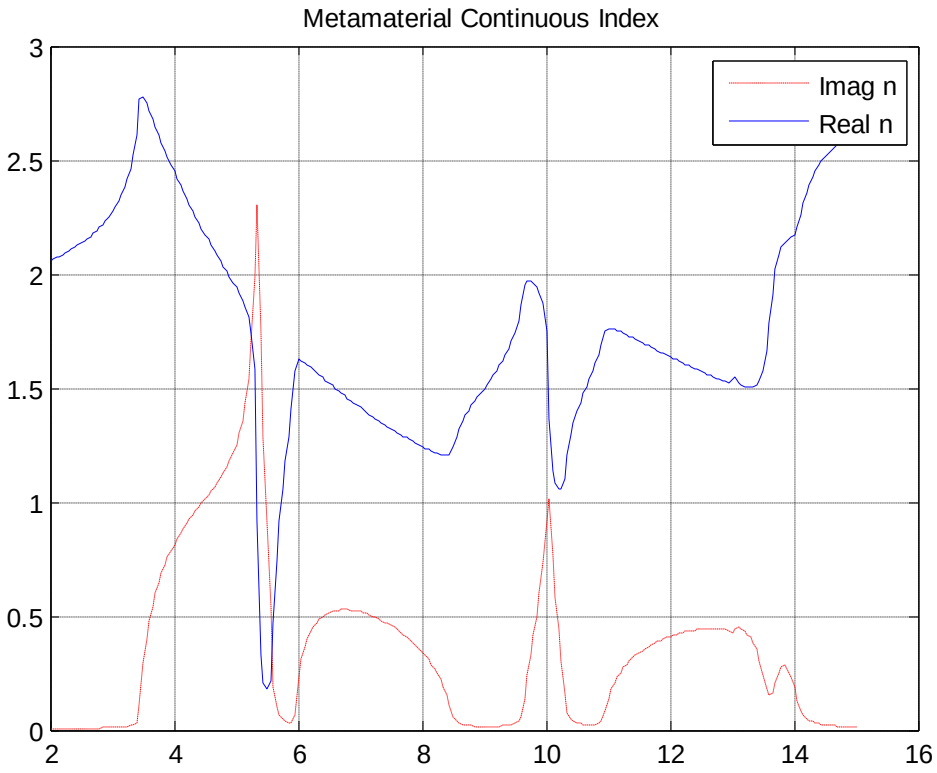

Figure 3.3.2: Continuous Metamaterial Refractive Index

It is seen that the imaginary part of the index is always positive, corresponding to the requirement for a passive system. This method of index retrieval was tested on a sample metamaterial structure, one published in [32]. The setup was identical to that used in [32] and used HFSS also. The original figures of retrieved parameters, using another method, will be shown followed by the retrieved parameters using the method here. The captions will include any discussions for individual comparisons.

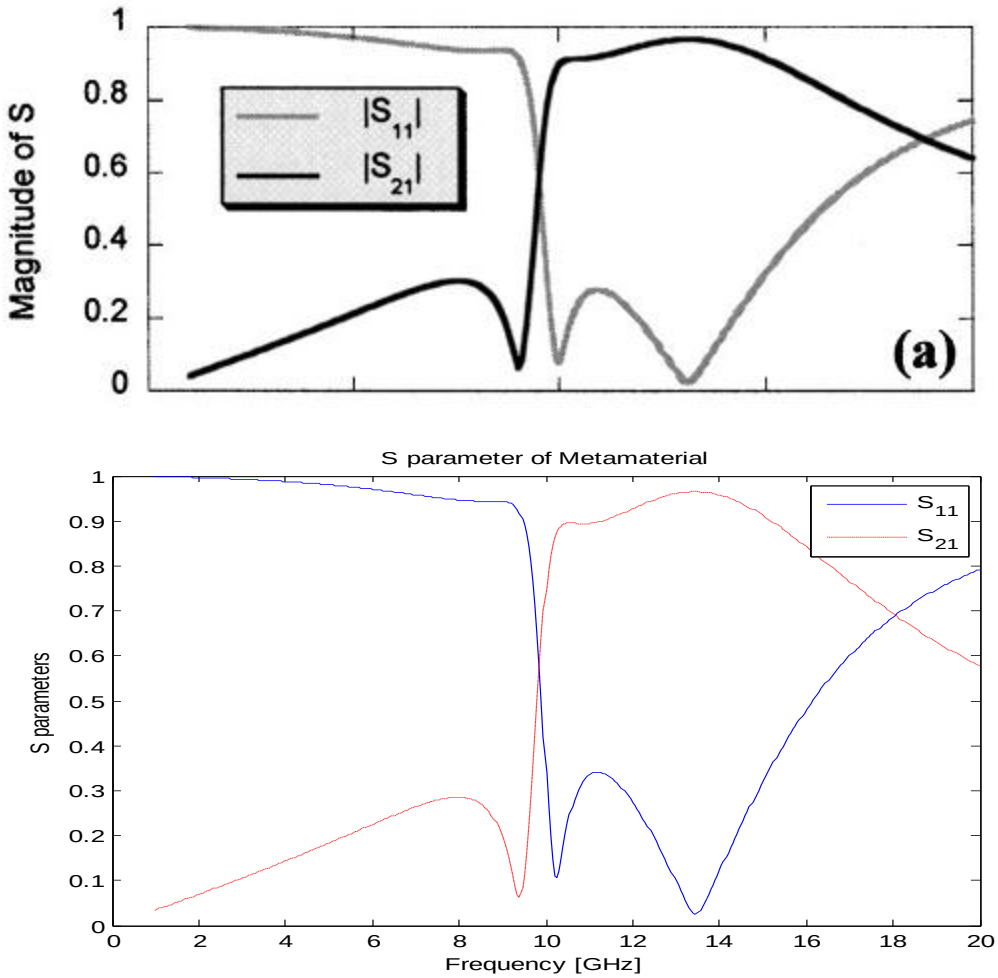

Figure 3.3.3: Magnitudes of S Parameters of Metamaterial. The top is the original figure from [32]. The bottom shows the results from the recreation, clearly showing that the simulation returned S parameter magnitudes extremely close to the originals.

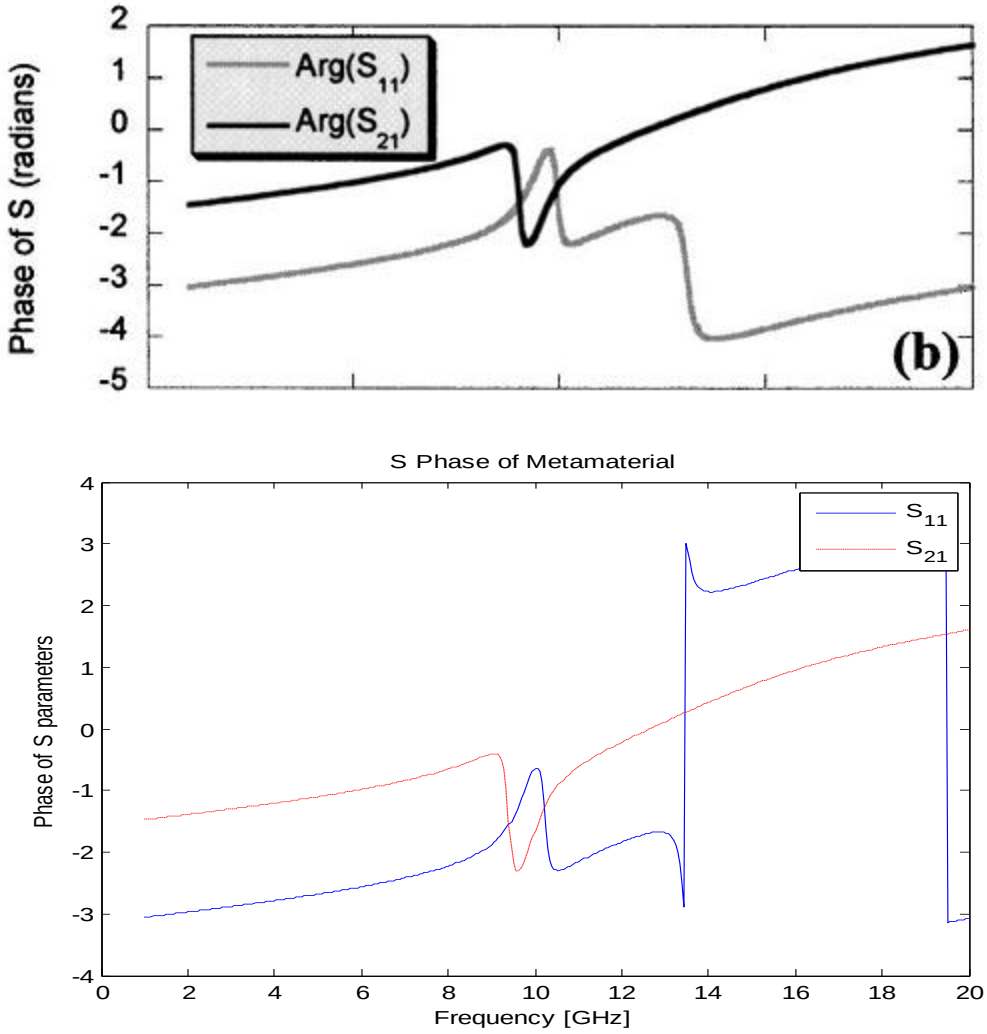

Figure 3.3.4: Phase of S Parameters of Metamaterial. The top is the original figure from [32]. The bottom shows the results from recreation. The discontinuity in the recreation around 13.5 GHz is due to the angle retrieval, where the recreation enforced angles only in the range [-π,π] while the original did not.

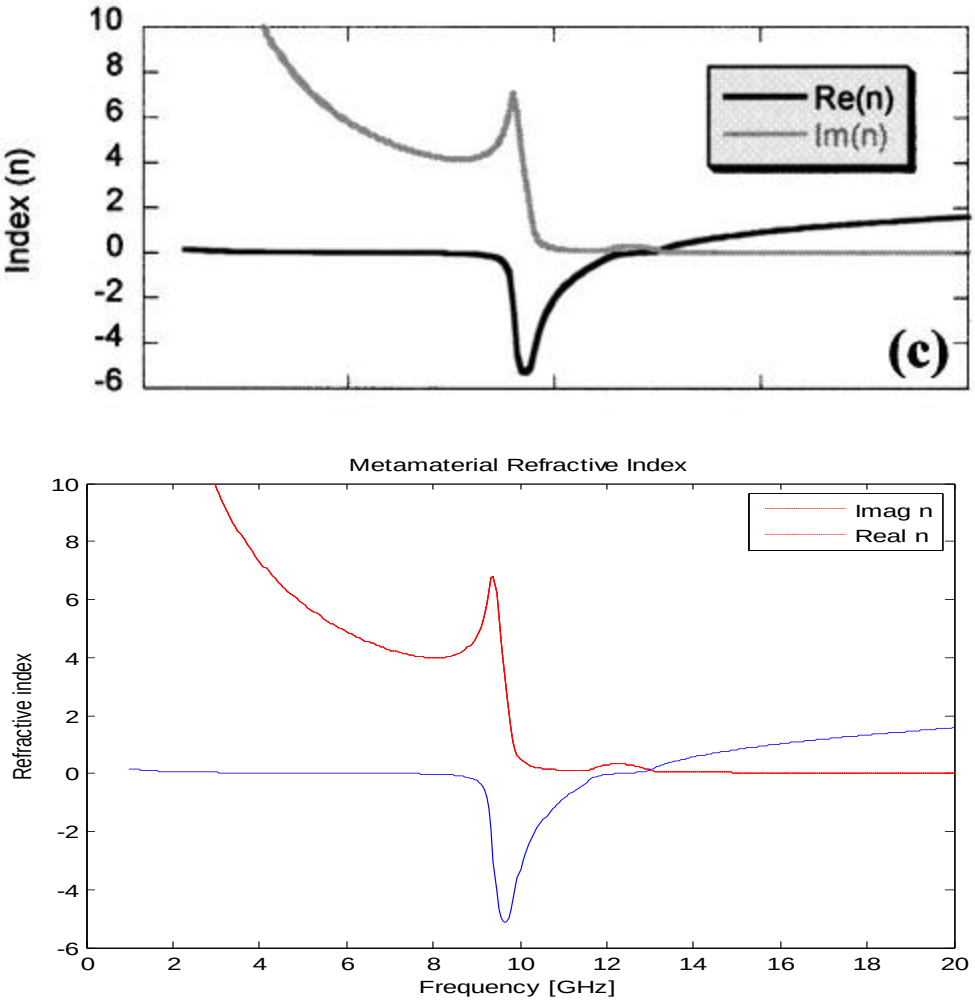

Figure 3.3.5: Extracted Index of Metamaterial. The top is the original from [32]. The bottom is the recreation and clearly shows excellent agreement with the original.

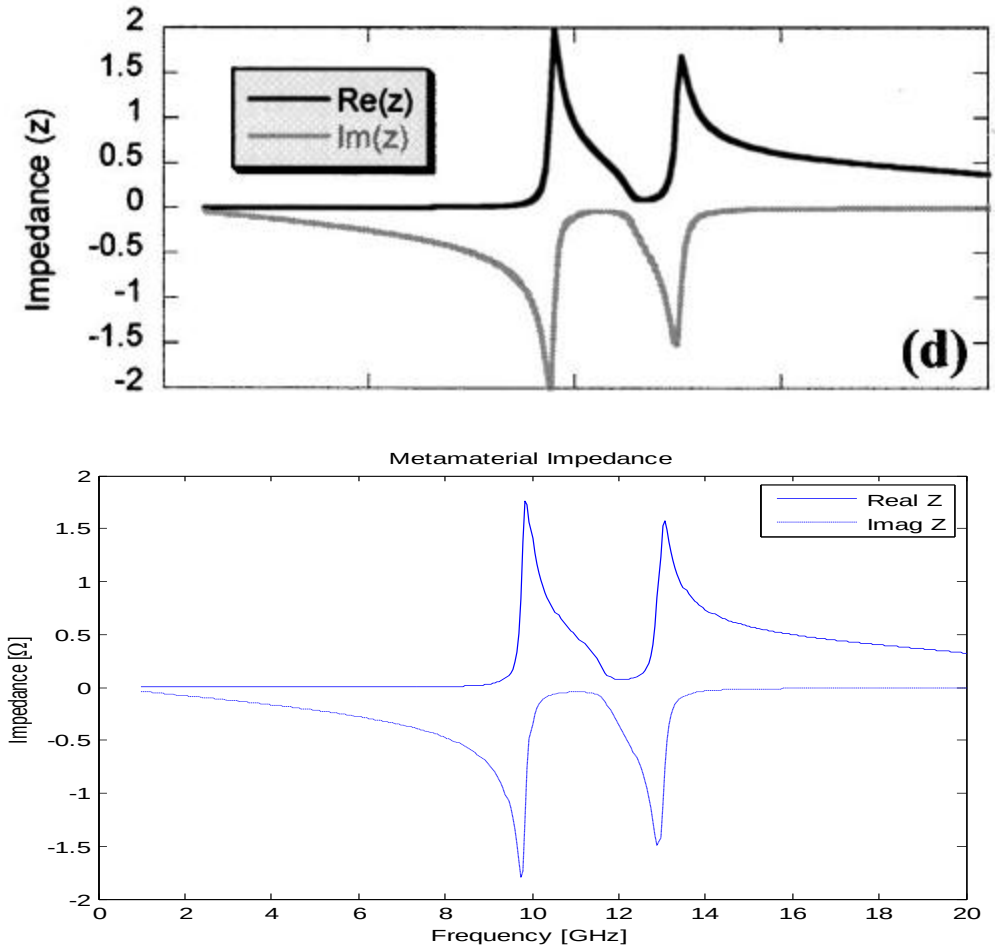

Figure 3.3.6: Extracted Impedance of Metamaterial. The top is the original from [32]. The bottom is a recreation and again clearly shows excellent agreement.

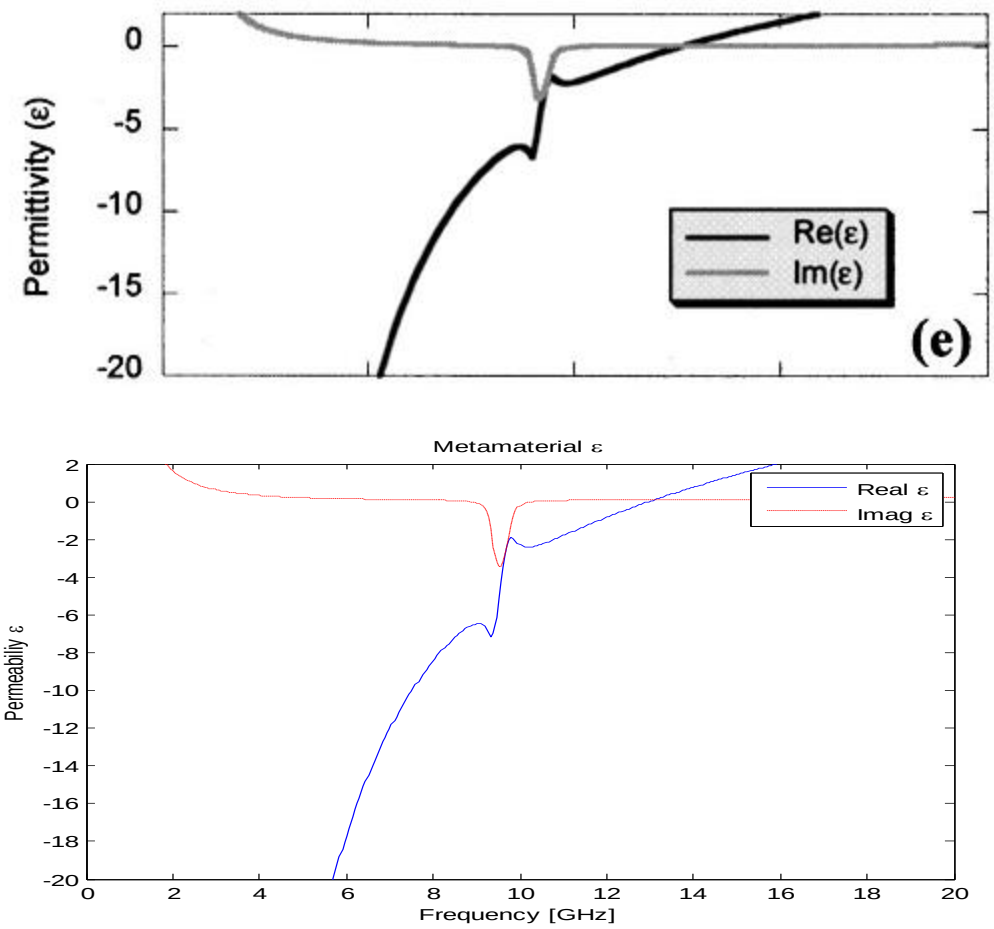

Figure 3.3.7: Extracted Permittivity of Metamaterial. The top is the original and bottom is recreation. Note that in both the imaginary part of ε can be positive or negative on the frequency range. The oft-stated requirement that the imaginary part be one sign to enforce passivity is not rigorously accurate. The requirement is that the imaginary part of the *index* be one sign to enforce passivity [33].

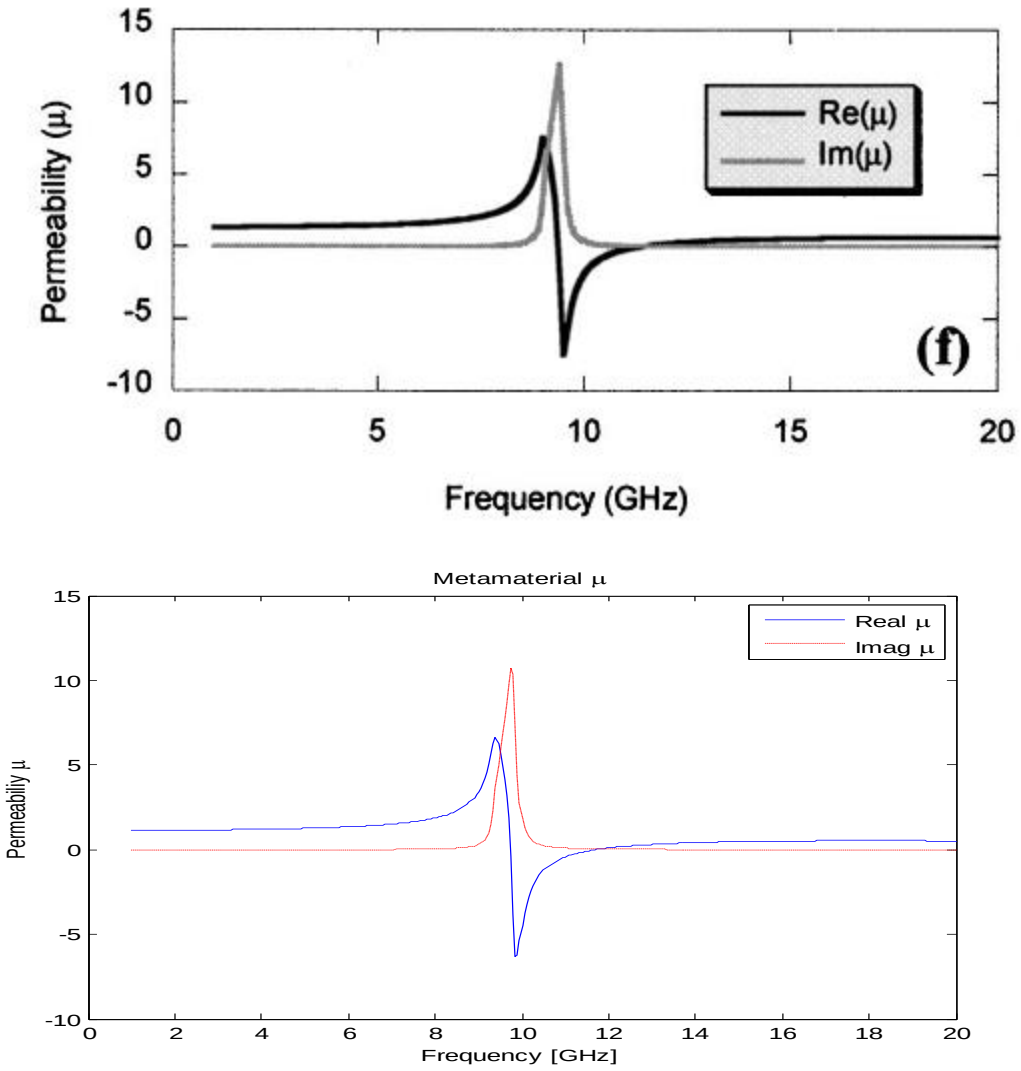

Figure 3.3.8: Extracted Permeability of Metamaterial. The top is the original, bottom is the recreation. The same note from Fig. 3.3.7 applies to the imaginary part of μ, although there are no sign changes for this metamaterial.

The preceding figures served to illustrate that the retrieval algorithm used here matches well with others and is able to reproduce published results. A sample segment of MATLAB code implementing this algorithm is included as Appendix C. Note that the Appendix does not include multiple thicknesses of samples, as the comparison was made with different simulations. The equation used to calculate the index parts was that given in [31] and is shown below.

$$n = \frac{1}{k_0 d}\left\{\left[\left(\ln\left(e^{ink_0 d}\right)\right)'' + 2m\pi\right] - i\left[\ln\left(e^{ink_0 d}\right)\right]'\right\} \qquad 3.3.4$$

It should be noted that this is the exact form of the equation used in [31] and, unfortunately, uses another notation as described previously. Going from an $e^{j\omega t}$ dependence to an $e^{-i\omega t}$ dependence changes the signs in the equations. However, this can be avoided by taking the complex conjugate of all S parameters simulated with a $e^{j\omega t}$ dependence, as illustrated in Appendix C. The general simulation setup for both this test and other parameter simulations will be detailed in the following chapter.

This chapter examined basic principles of negative index metamaterials. Effective material analysis was also examined, including both venerable techniques like NRW and newer approaches. Limitations with traditional retrieval techniques with regard to metamaterials were discussed and analyzed. These limitations were overcome by enforcing continuity of the material parameters and enforcing passivity. The retrieval method was implemented and successfully duplicated published results for a negative index metamaterial. The following chapter will go a step further and consider metamaterial structures, rather than homogeneous media as in this case.

Chapter 4: Metamaterial Constitutive Particles

4.1 Existing Particle Review and Simulation Techniques

The previous chapter considered metamaterials as effectively homogeneous media. The essence of creating a metamaterial, however, is realizing a subwavelength structure. This subwavelength structure will not have the same properties as a metamaterial when the wavelength is comparable to the size of the structure. One of the most important questions in metamaterial research today is how to create more and more flexible particles with different properties of interest. As discussed in the previous chapter, artificial structures that have negative effective permittivity are rather venerable and well-understood. An important point is that they are also very easy to fabricate and extend to make isotropic metamaterials. Negative permittivity is often realized by a simple array of wires, whether in two or three dimensions. Generally, inductive-like structures can be used. Structures like capacitively-load strips [17] and other similar structures may be used rather than simple straight wires. However, negative permeability is somewhat more difficult to realize. This is because, as realized in [11], structures giving negative permeability should act like a "magnetic plasma." Because such a thing does not exist in nature, it is more difficult to imagine structures that exhibit such behavior. The first structure to exhibit negative permeability, the SRR, is still the most popular. SRRs are fully scalable with frequency [33]. Due to their nature, however, they are resonant structures. Typical SRRs only have one resonance, so they only have one narrow band with negative permeability. They are also somewhat lossy in the resonance band. Several different methods of creating multiband structures have been proposed [34,35] that rely on SRRs or SRR-like structures. Reference [34] utilizes pairs of SRRs of

different sizes for multiple bands. Reference [35] analyzes the complementary electric LC (CELC) resonator for use in frequency-selective surfaces (FSS). Another recent effort has utilized a cross-based structure to create a metamaterial with either negative index or negative permittivity for use in higher frequency applications [36]. Despite these recent efforts, however, the toolbox of magnetic (negative permeability) metamaterial structures remains small.

One of the main problems with SRR-based metamaterials is that they are not rotationally-independent. A new particle, described in the following sections, was designed and analyzed to be significantly less rotationally-dependent. The particle was also designed with the goal of having increased bandwidth and/or multiple bands with negative effective material parameters. The following section will discuss the simulation tools and methods used, while subsequent sections will discuss and present findings for new metamaterial structures.

4.2 Simulation Setup

The setup used to simulate a metamaterial is very important and somewhat dependent on the numerical tool used. HFSS was used for all numerical simulations and is an industry standard for electromagnetic simulations. The very nature of metamaterials requires that there be an array of "particles." Ultimately metamaterials are volumetric in nature, so designs may be volumetric in simulations, as well. However, volumetric simulations require tremendous computational resources and are not frequently conducted for first designs. The most common and efficient type of simulation considers an infinite two-dimensional array. The question is generally how to simulate a plane wave impinging on an infinite two-dimensional array, since that is what is generally desired for non-conformal applications. Inductive and wire arrays, as electric elements, are excited by an electric field tangential to the individual elements. Magnetic particles, like SRRs and any others with similar structural features,

are excited by a magnetic field normal to the plane of the individual elements. Thus, if arranged correctly, a full metamaterial can be excited by a TEM plane wave.

There are two main issues with the basic simulation setup. The first is the simulation of an infinite array in the most efficient way. The second is the simulation of a plane wave. These two goals can be accomplished simultaneously through the use of appropriate boundary conditions. Perfect electric conducting (PEC) boundary conditions force the tangential electric field to zero [19]. Similarly, perfect magnetic conducting (PMC) boundary conditions, although not physically realizable, force the tangential magnetic field to zero. When arranged appropriately, PEC and PMC boundaries force the electric and magnetic fields to be TEM. Moreover, image theory [19] combines with this effect to simulate an infinite two-dimensional array. The PEC is arranged to be normal to the desired electric field and the PMC is arranged to be normal to the desired magnetic field. The proper arrangement in two dimensions is shown below in figure 4.2.1.

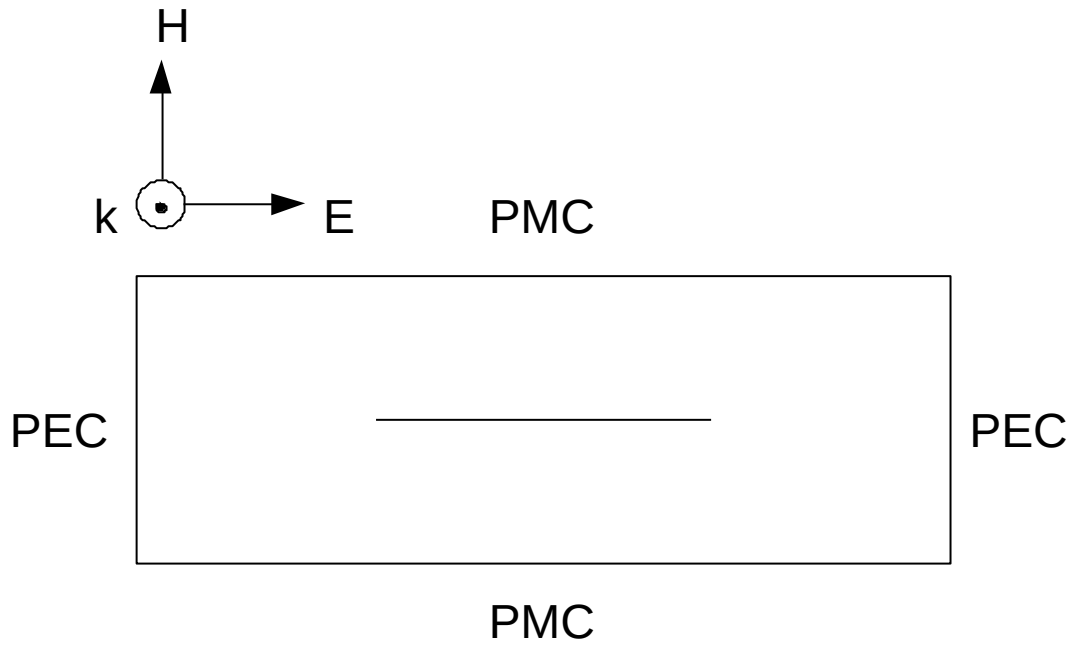

Figure 4.2.1: Arrangement of Boundary Conditions for Unit Cell

This arrangement creates a plane wave as shown. When extended in three dimensions along the *k* vector, this arrangement simulates an infinite array in the plane of the page. Thus, the two requirements mentioned previously have both been satisfied through the use of appropriate boundary conditions. The question then becomes how to enforce a plane wave at each port which is on the exterior of the unit cell.

HFSS has several options of excitation types depending on the excitation desired. The most appropriate for this type of simulation is one which can support a plane wave mode, as shown above, and one which can obtain transmission and reflection coefficients or S parameters. The most appropriate one for HFSS is the wave port. The wave port simulates a semi-infinite waveguide terminating at the selected face. The default modes from this excitation are those corresponding to an all-PEC waveguide, the fundamental of which is a half-sine distribution. With certain boundary conditions, however, HFSS forces the modes in the waveguide to match those of the used boundary conditions. In other words, with the PEC-PMC arrangement used here, HFSS forces a mode for a PEC-PMC waveguide – a plane wave. The wave port excitation also automatically calculates S parameters for the structure. The convergence setup used in HFSS with a wave port excitation refines the mesh and checks the S parameters against values from less refined mesh. When the difference is below a specified value, the simulation has converged. The default (and value used here) is 0.02 or 2%. For increased accuracy the simulator was forced to obtain three consecutive converged passes for true convergence. When simulating over a band of frequencies, a single solution frequency is chosen at the upper end of the band of interest. This frequency is the one used for refinement of the mesh and a convergence test. This refined mesh is then used for all the other frequencies of interest.

A further issue can arise when simulating such a structure. The finite extent of the structure along the direction of propagation can introduce errors in evanescent waves. One way to remove errors

from this effect is to make the size of the simulation domain slightly larger than the actual unit cell along the direction of propagation. Since this alters the S parameters of the structure, it must be compensated for. A post-processing option included in HFSS is used for this. The S parameters are deembedded from the simulated boundary to the edge of the unit cell. Deembedding S parameters is a well-known and venerable practice [4], but is only effective when no discontinuities are between the original boundary and the deembedded boundary. This is not a problem in this simulation as the only material between the two boundaries is a uniform dielectric with no discontinuities.

For the simulations conducted in subsequent sections, some other choices were made for simplification. To reduce simulation time, all metal traces were rendered as two-dimensional sheets. To retain some of the accuracy, however, the traces were set as copper, with a conductivity $\sigma = 5.8 * 10^8 \frac{S}{m}$, to include some loss effects. A dielectric substrate was also used for all simulations. The dielectric used was Dupont 951 Green Tape. Relevant parameters for this include $\mu_r = 1$, $\varepsilon_r = 7.8$ at 3 GHz, and $\tan(\delta) = 0.006$ at 3 GHz [37]. The dimensions will be discussed with individual structure simulations. This section has now described all the necessary simulation parameters and setup used for subsequent simulations. The following sections will actual new particles and the results.

4.3 New Particle Study: Jerusalem Crosses In Place of Traditional SRRs

Most existing magnetic metamaterial structures are based on SRR characteristics. Even though many structures have been developed, there are an infinite number that contain SRR characteristics. One structure that has not been considered as a metamaterial particle is a Jerusalem Cross (JC), an example of which is picture in figure 4.3.1 below.

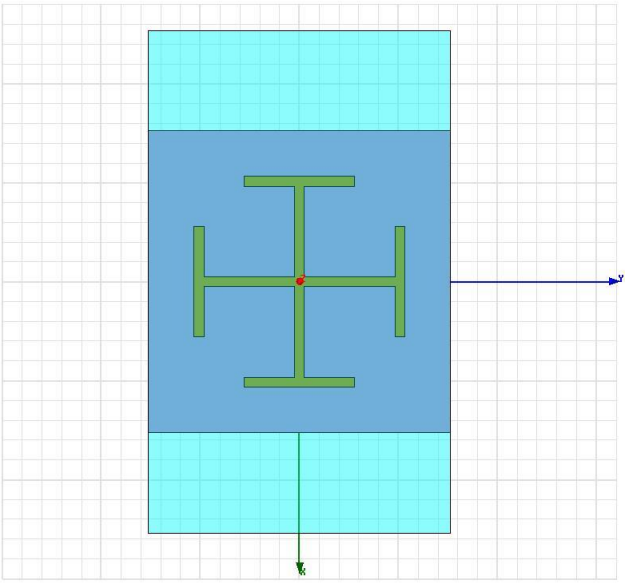

Figure 4.3.1: Sample JC Picture

The JC has been used in frequency-selective surfaces (FSS) for years [e.g. 38]. Unlike the setup described in the previous section, however, FSS using JCs are arranged as single-layer surfaces. The wave propagation direction is normal to the plane of the JC, normal to the page in the view of figure 4.3.1. When designed correctly FSS can produce surfaces with high impedance for selected frequencies. However, creating volumetric objects such as metamaterials can produce different effects. JC-based metamaterials have not been studied to this point. The closest structure is that of [39], which combines the general FSS approach with the bulk metamaterial approach. In this structure the propagation vector is still normal to the plane of the JC, as in an FSS, but periodic layers of JCs are used to obtain metamaterial behavior. The behavior of a metamaterial structure with JCs substituted for SRRs has not been studied thus far and will be studied here. The first simulated structure used the setup described in the previous section with the structure pictured below in figure 4.3.2.

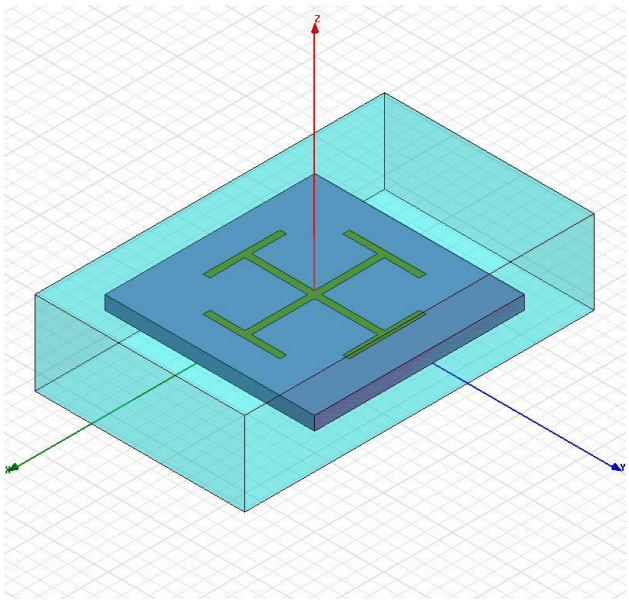

Figure 4.3.2: Layout of Initial JC for study

As shown here the propagation direction is along the negative *x*-axis. The dielectric layer is Dupont 951 and is 40 mils thick. The copper traces are each 20 mils wide, with the total unit cell size 600x600x240 mils. The cell as shown is slightly larger along the propagation direction for deembedding the S parameters as described previously by a distance of 100 mils on each side. A structure with part of the features of a JC has been studied and shown to yield solely electric behavior in [17]. The following pages will present the simulated results (S parameter magnitudes and phases) and extracted parameters, beginning in figure 4.3.3. The retrieval procedure used was that described in the previous chapter.

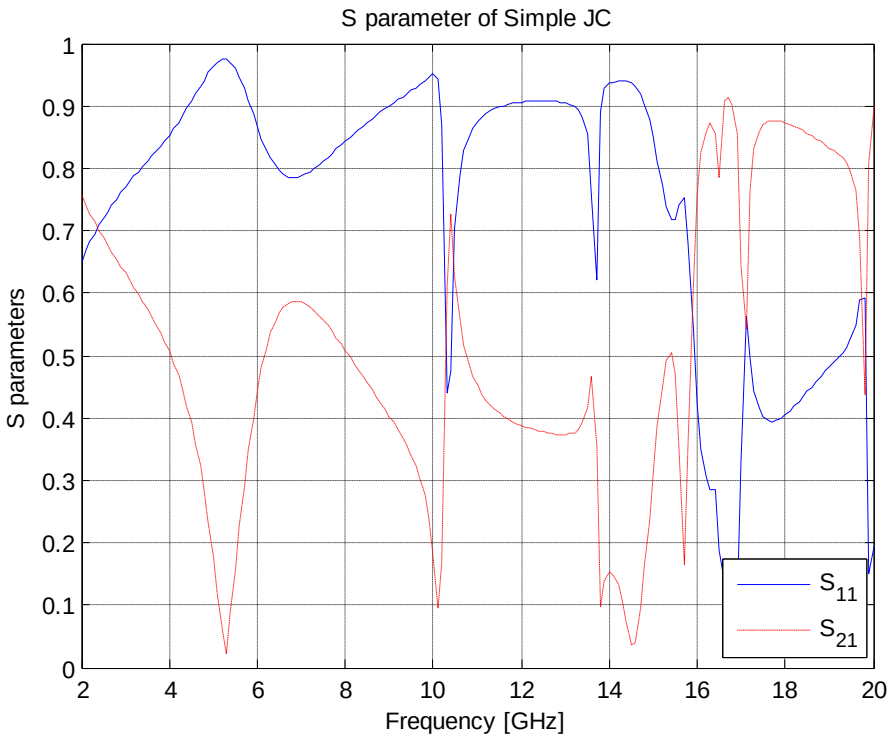

Figure 4.3.3: S Magnitudes for Simple JC

Note the characteristic metamaterial-like behavior of a dip in S_{21} at multiple frequencies.

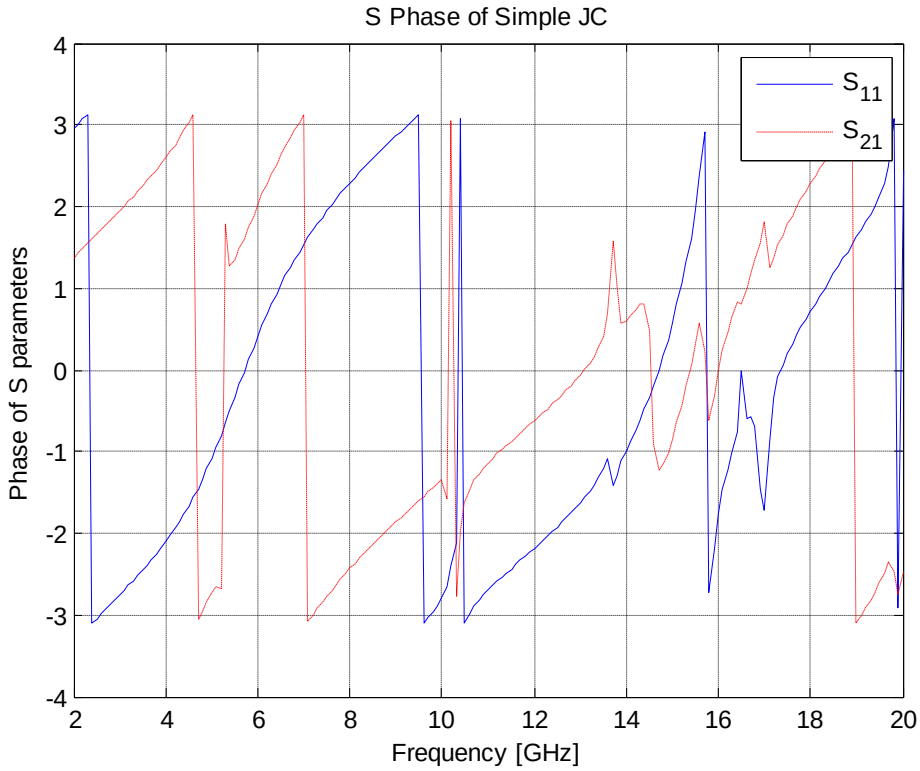

Figure 4.3.4: S Phases for Simple JC

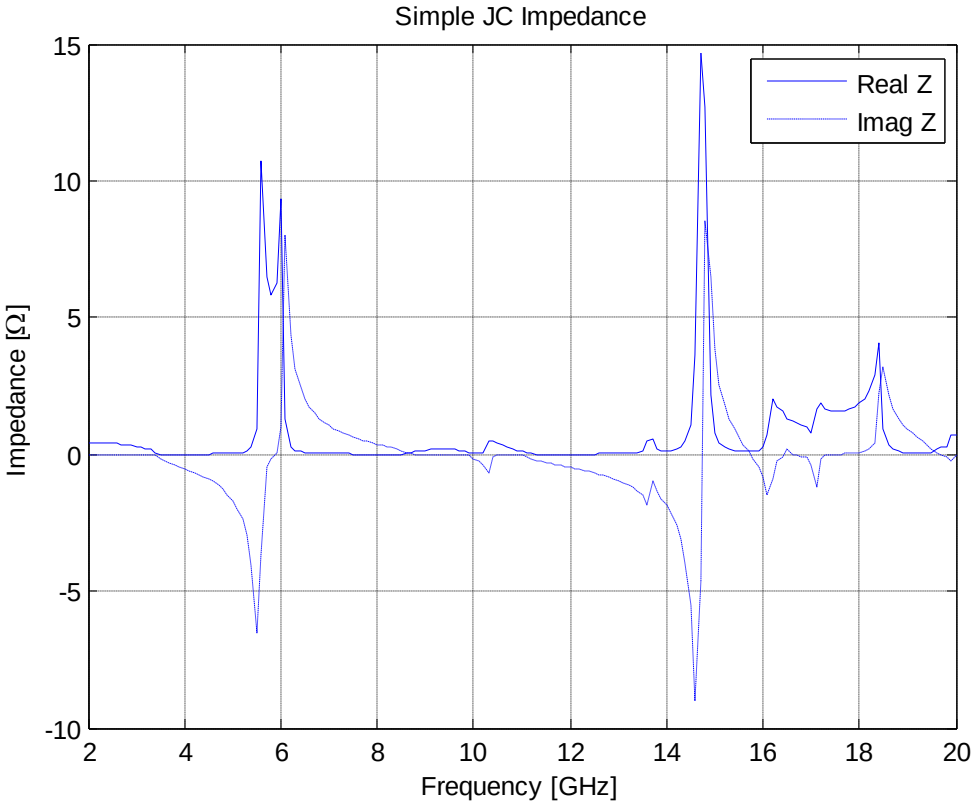

Figure 4.3.5: Extracted Simple JC Impedance

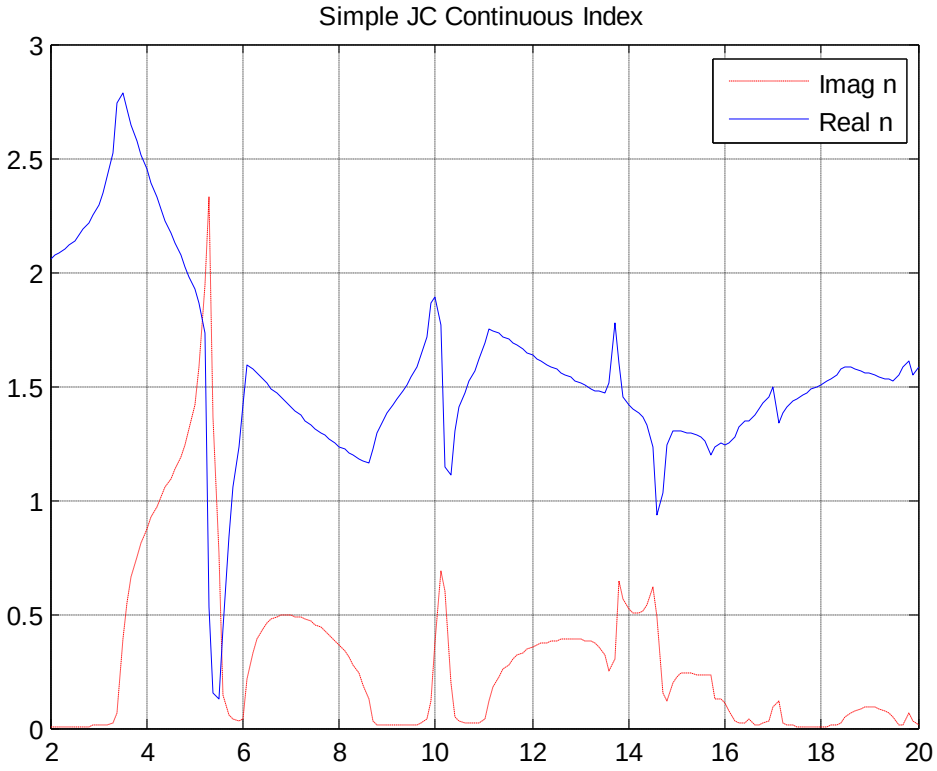

Figure 4.3.6: Extracted Simple JC Refractive Index

Since this structure is intended to only exhibit negative values for one of the two parameters (μ and ε), the index should not have negative values, and this is shown here. The large dip in the real part of the index around 5.5 GHz corresponds to interesting behavior as shown in the following figure.

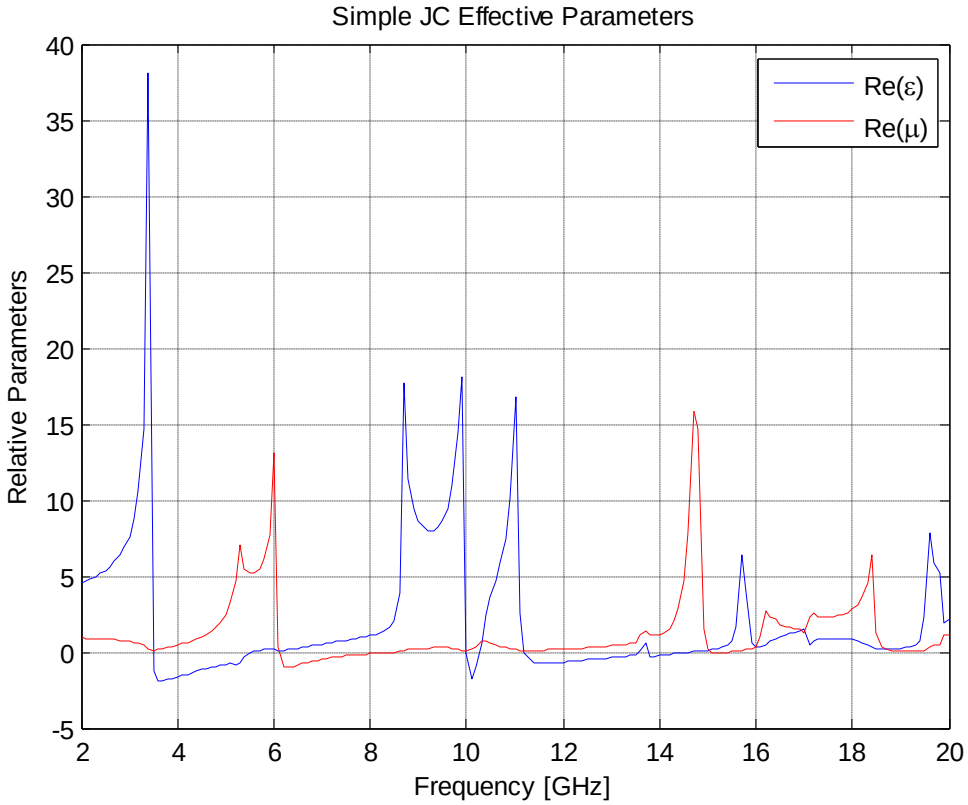

Figure 4.3.7: Extracted Parameters for Simple JC

There are multiple regions of interest from the metamaterial point of view shown here. First, this structure exhibits both negative permeability and permittivity in different frequency bands. Negative permittivity is shown between about 3.5 and 5.5 GHz; 10.0 and 10.25 GHz; 11.25 and 13.5 GHz; and 13.75 and 14.6 GHz. This is very unusual behavior for traditional negative permittivity structures. In fact, the small positive band in the region of 13.5-13.75 GHz could be due to a small simulation error. As was illustrated in the previous chapter, simple wire arrays exhibit a negative permittivity below a certain frequency and a positive permittivity above. This structure is unique in that it possesses multiple bands of negative permittivity and in that the bands do not show the traditional dipole behavior, where the permittivity is negative below a certain resonant frequency. This alone is unique to the author's knowledge in the design of electric metamaterials. Moreover, this structure possesses a very clear negative-permeability band from about 6.2 to 8.55 GHz. This is a bandwidth of 31.86%, significantly

larger than traditional SRR structures as in the previous chapter, which exhibited a bandwidth of about 18%. This new structure provides great flexibility and enables the possibility of more multiband structures while using a simple structure that is very simple to fabricate. This structure provides unique features for metamaterial design especially with the combination of electric and magnetic responses at different frequencies. Moreover, the nature of the JC allows interchanging the propagation and electric field vectors without affecting the structure's electromagnetic response, an unusual feature not present in most SRR-derived structures. It is expected that the structure should be scalable.

The basic structural features of JCs allow a relatively simple extension to a fractal type of geometry. A fractal JC is shown below in figure 4.3.8.

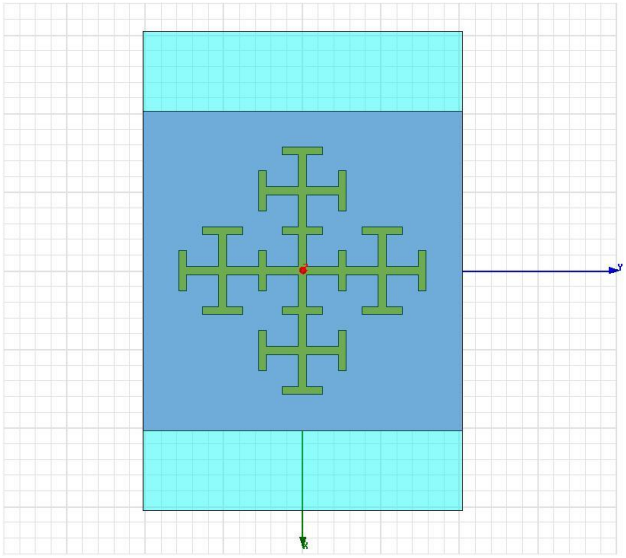

Figure 4.3.8: Geometry of Fractal JC

This structure is very similar to the JC previously shown. In fact, the fractal elements of the geometry were added directly to the original JC presented earlier. This necessitated a slight increase in the size of the unit cell to ensure that the structure was entirely contained within it, from a unit cell size of 600x600x240 mils to 800x800x240 mils. Otherwise the simulation parameters were as listed before. The additional fractal elements were expected to create additional inductive and capacitive resonances,

especially at higher frequencies, so the response was analyzed as before. The extracted parameters for this structure are shown below in figure 4.3.9.

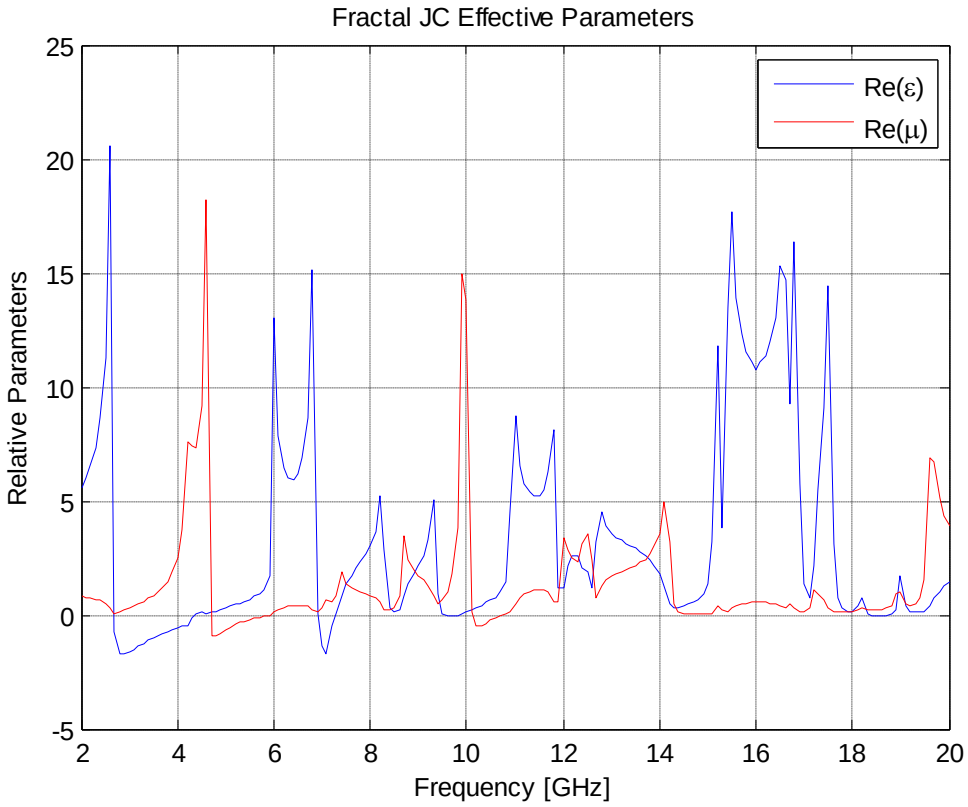

Figure 4.3.9: Extracted Parameters for Fractal JC

This structure has similar features to the simple JC at some frequencies. The introduction of the different size unit cell led to a frequency shift: as has been shown in some of the literature, the lattice size of a metamaterial is closely related to its response. The larger lattice size shifts the response lower in frequency. The extracted parameters for the simple and fractal JCs are shown in figures 4.3.10 and 4.3.11 below.

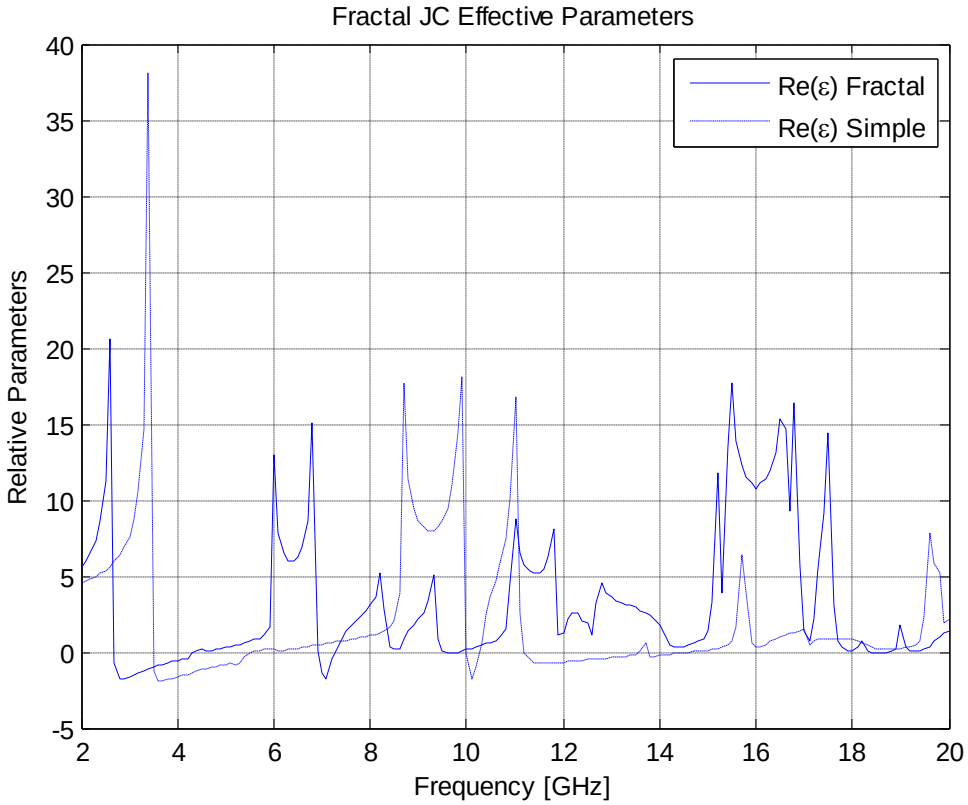

Figure 4.3.10: Extracted Permittivity for Jerusalem Cross Structures

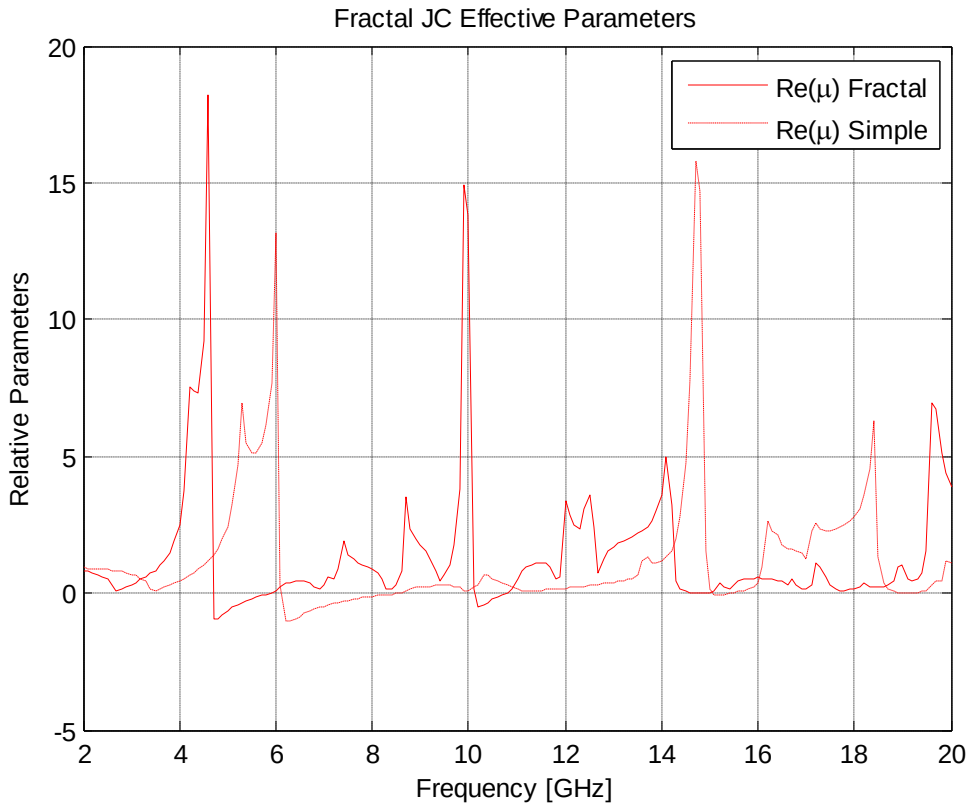

Figure 4.3.11: Extracted Permeability for Jerusalem Cross Structures

Some interesting points arise. First, as mentioned, the features are shifted down in frequency with the larger unit cell size for both material parameters. The shift in frequency also somewhat compresses the features, leading to smaller bandwidths for some features. However, the interesting additional electromagnetic features from the fractal geometry arise at the higher end of the frequency range. The fractal features alter the electric response by eliminating one of the negative bands of permittivity effectively. The larger change, however, is the addition of another band of negative permeability. Through use of fractal geometric features, this structure attains multiple bands of both negative permittivity and permeability, a unique feature in the designer's toolbox of metamaterial structures. The flexibility presented by the frequency bands of interest is very interesting. However, the

negative regions were rather close to zero, and could hence be due to numerical errors. A more resonant structure was simulated to analyze this and is pictured below.

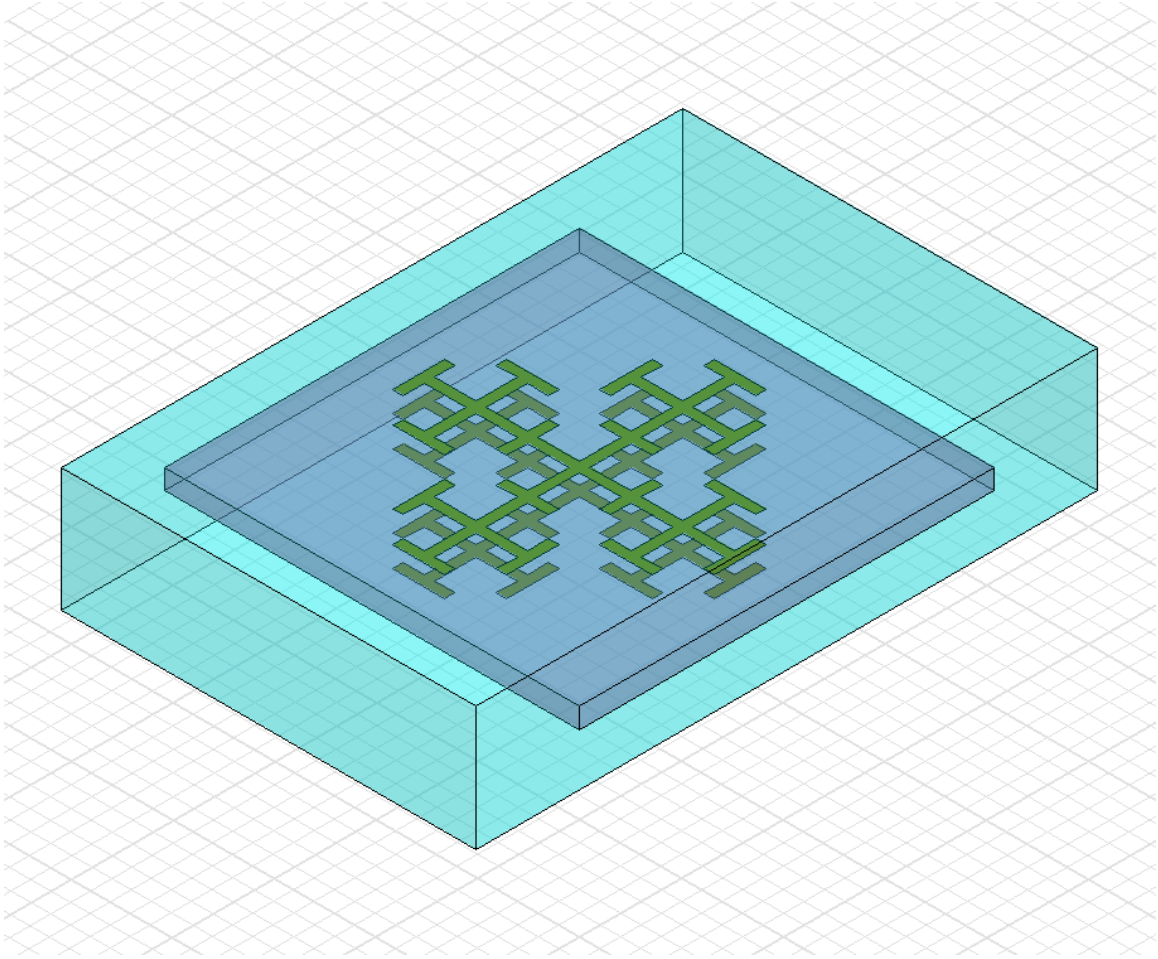

Figure 4.3.12: Double Fractal JC Cell

This structure uses an identical fractal JC, but has the JC printed on both sides of the dielectric slab. This does not affect the band structure much, as will be shown shortly, but does increase the peaks of the resonances. The extracted material parameters are shown below for the double fractal JC.

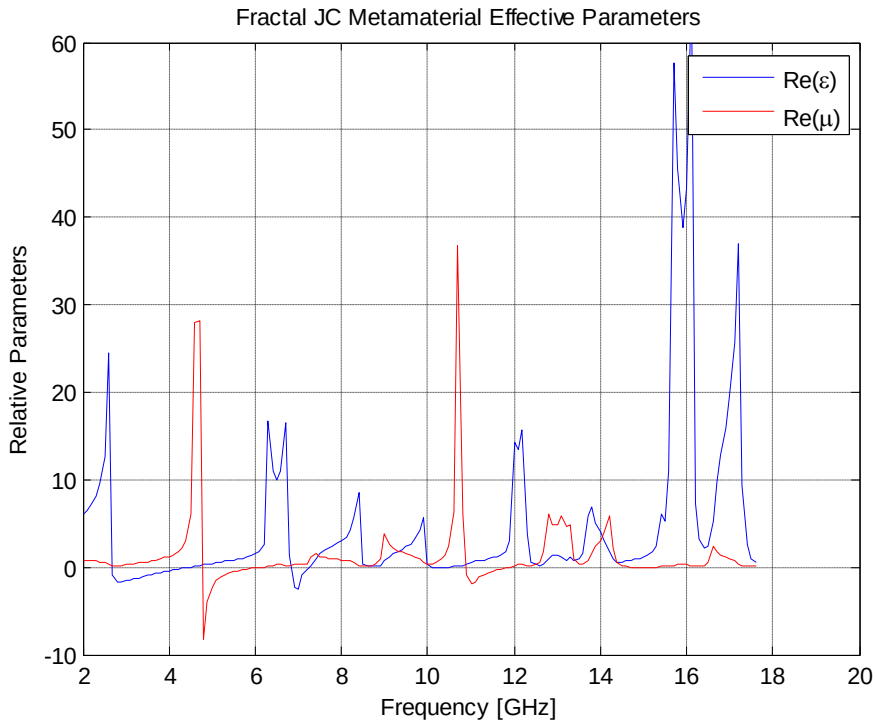

Figure 4.3.13: Extracted Material Parameters for Double Fractal JC

A comparison of this and Figure 4.3.9 shows that the resonances do not move in frequency, leading to a hypothesis that coupling is not very significant with the arrangement simulated here. More importantly, however, is the fact that the peaks are more pronounced. This validates the existence of multiple bands of negative permittivity and permeability, since the peaks are no longer very close to zero and, hence, likely not due to numerical errors from the simulation.

This structure is not perfect, however. One of the main issues is the fact that the negative bands of permittivity and permeability do not overlap at all. Negative permeability and permittivity are very important but only in the sense that they enable a negative index, and negative index requires both material parameters to be negative. Further research is being conducted to study whether different sizes of fractal JCs can be combined in the same unit cell where the bands have been designed to overlap. Also, as in all resonant structures, the fractal JC is lossy in the regions of interest. This can be

seen by examining the imaginary part of the index in the negative parameter bands. This is a feature that is present in resonant structures and is one of the fundamental problems with current metamaterial research. Another issue requiring further study for the fractal JC is introduced by the fractal geometrical features. The fractal features were added to give multiple higher-order negative permeability bands, and this effort was successful. The fractal elements add interesting behavior at higher frequencies. However, at higher frequencies the interpretation of the metamaterial as an effectively homogeneous medium is not valid. Treating a structure as homogeneous assumes that its structural features are smaller than the wavelength. For the fractal JC, the unit cell is 800 mils long, which is equivalent to a frequency of 14.76 GHz. Above this frequency the Subwavelength assumption no longer holds and, hence, the metamaterial assumption is no longer valid. Higher frequency behavior of the fractal JC (and higher order fractal geometries) are under further study.

Despite the aforementioned issues, this structure enables more flexibility in designing metamaterials, particularly since the fractal JC exhibits multiple frequency bands with positive and negative permeability and permittivity. It is expected that optimization of the JC and fractal JC dimensions could yield even larger bandwidths of negative permittivity or permeability and this is still under investigation. Current efforts are also focused on the scalability of JCs and fractal JCs. It is expected that appropriate large structures of JCs and fractal JCs could match the negative permittivity and permeability bands of different JC elements, yielding negative index solely through the appropriate use of JC structures. Further investigations will also consider rotational dependence of the JC, since it is known that the structure is rotationally symmetric along 90° increments.

Chapter 5: Conclusions

Engineering at radio frequencies has become a ubiquitous field over the past several decades. The differences between RF engineering and low frequency engineering are numerous and require new tools. These new tools include different types of electromagnetic analysis, analyzed in the second chapter of this thesis. Not only is it often advantageous to be able to write simulation code rather than using a commercial package, but knowledge of the different simulation algorithms and their limitations is a requirement for conducting efficient simulations. Anyone can envision a structure that might or might not have interesting properties. Often, however, a structure can only be tested by a seasoned electromagnetic designer. Attempts to simulate structures using incorrect boundary conditions or even incorrect simulation algorithms can lead to huge decrease in efficiency and incorrect results. High-Q or highly resonant structures, for instance, should not be simulated using time-domain simulation algorithms for efficient tests. Issues such as these were examined in the second chapter of this thesis.

Tools for RF engineering also include effective material and network analysis. Without robust, efficient material parameter retrieval techniques, the only data gathered from a simulation may be whether or not a structure allows transmission. This is not sufficient, for structures may have stopbands for numerous reasons. To this end parameter retrieval algorithms were analyzed and an effective, stable one was implemented.

A new tool of the last decade or so is the ability to create structures with effective permeabilities and permittivities with any desired value. This ability is essential to the creation of

cloaking devices, for example. The metamaterial designer's toolbox of fundamental structures is still very empty and a need exists for multiband structures in particular. Existing structures were discussed and analyzed and new ones were developed. Structures based on a Jerusalem Cross were implemented, simulated, and analyzed to study their electromagnetic properties in novel configurations. It was found that JC structures offer multiple bands of negative permittivity and permeability, a phenomenon not found in previous structures. Moreover, the structure of higher-order JC structures such as the fractal design studied permit even greater flexibility in engineering new materials. Metamaterials with multiple bands of negative permittivity and multiple bands of negative permeability were analyzed and validated by simulation. Further directions of research were opened up by this initial study. JC-based metamaterial structures offer flexibility not found in existing metamaterial structures and this study has offered initial characterization of JC structures. The properties found in fractal JC structures are also unique and will provide avenues for future research. The structures studied and characterized in this thesis will provide more tools for the metamaterial and RF designer and allow new designs with greater flexibility.

References

[1] – C.A. Balanis. *Antenna Theory Analysis and Design*. Wiley-Interscience, 3rd ed, Hoboken, NJ. 2005.

[2] – B. Razavi. *RF Microelectronics*. Prentice Hall PTR, Upper Saddle River, NJ. 1998.

[3] – C. Bowick. *RF Circuit Design*. Newnes, Indianapolis, IN. 1982.

[4] – D. Pozar. *Microwave Engineering*. John Wiley, 3rd ed. 2004.

[5] – M.N.O. Sadiku. *Numerical Techniques in Electromagnetics*. CRC Press, 2nd ed, New York. 2001.

[6] – A.S. Sedra, K.C. Smith. *Microelectronic Circuits.* Oxford University Press, 5th ed, New York. 2004.

[7] – P. Bhattacharya. *Semiconductor Optoelectronic Devices*. Prentice Hall, 2nd ed, New Jersey. 1997.

[8] – W.E. Kock. "Metallic Delay Lenses." *Bell Sys. Tech. J*. vol. 27, pp. 58-82, 1948.

[9] – W. Rotman. "Plasma simulation by artificial dielectrics and parallel-plate media." *IRE Trans. Ant. Prop.* vol. AP-10, no. 1, pp. 82-85, 1962.

[10] – J.B. Pendry, A.J. Holden, D.J. Robbins, W.J. Stewart. "Magnetism from conductors and enhanced nonlinear phenomena." *IEEE Trans. MTT*. vol. 47, no. 11, 1999.

[11] – V.G. Veselago. "The electrodynamics of substances with simultaneously negative values of ε and μ." *Sov. Phys. Usp*. vol. 10, no. 4, pp. 509-514, 1968 (Translated from original Russian).

[12] – R.A. Shelby, D.R. Smith, S. Schultz. "Experimental verification of a negative index of refraction." *Science* vol. 292, pp. 77-79, 2001.

[13] – A.M. Nicolson, G.F. Ross. "Measurement of the intrinsic properties of materials by time-domain techniques." *IEEE Trans. Instr. and Meas*. vol. IM-19, no. 4, pp. 377-382, 1970.

[14] – W.B. Weir. "Automatic measurement of complex dielectric constant and permeability at microwave frequencies." *Proc. of the IEEE* vol. 62, no. 1, pp. 33-36, 1974.

[15] – J.B. Pendry. "Negative refraction makes a perfect lens." *Phys. Rev. Lett*. vol. 85, no. 18, pp. 3966-3969, 2000.

[16] – D. Schurig, J.J. Mock, B.J. Justice, S.A. Cummer, J.B. Pendry, A.F. Starr, D.R. Smith. "Metamaterial electromagnetic cloak at microwave frequencies." *Science* vol. 314, pp. 977-980, 2006.

[17] – R.W. Ziolkowski. "Design, fabrication, and testing of double negative metamaterials." *IEEE Trans. Ant. and Prop*. vol. 51, no. 7, pp. 1516-1529, 2003.

[18] – T.H. Hand, J. Gollub, S. Sajuyigbe, D.R. Smith, S.A. Cummer. "Characterization of complementary electric field coupled resonant surfaces." *Appl. Phys. Lett.* vol. 93, pp. 212504 1-3, 2008.

[19] – C.A. Balanis. *Advanced Engineering Electromagnetics*. John Wiley. 1989.

[20] – D.M. Sullivan. *Electromagnetic Simulation Using the FDTD Method*. John Wiley, New Jersey. 2000.

[21] – A. Taflove, S.C. Hagness. *Computational Electrodynamics: The Finite-Difference Time Domain Method*. Artech House, 3rd ed, Norwood MA, 2005.

[22] – R.W. Ziolkowski, E. Heyman. "Wave propagation in media having negative permittivity and permeability." *Phys. Rev. E* vol. 64, 056625 1-15, 2001.

[23] – K.S. Yee. "Numerical solution of initial boundary value problems involving Maxwell's equations in isotropic media." *IEEE Trans. Ant. and Prop*. vol. AP-14, no. 3, pp. 302-307, 1966.

[24] – R.W. Ziolkowski, A.D. Kipple. "Causality and double-negative metamaterials." *Phys. Rev. E* vol. 68, 026615 1-9, 2003.

[25] – G.V. Eleftheriades, K.G. Balmain (editors). *Negative-Refraction Metamaterials: Fundamental Principles and Applications*. John Wiley, New Jersey. 2005.

[26] – N. Kundtz, D.A. Roberts, J. Allen, S. Cummer, D.R. Smith. "Optical source transformations." *Optics Express* vol. 16, no. 26, pp. 21215-21222, 2008.

[27] – Y. Luo, J. Zhang, L. Ran, H. Chen, J.A. Kong. "New concept conformal antennas utilizing metamaterial and transformation optics." *IEEE Ant. Wireless Prop. Lett.* vol. 7, pp. 509-512, 2008.

[28] – F.T. Ulaby. *Fundamentals of Applied Electromagnetics*. Pearson Prentice Hall, 2004 Media ed, New Jersey. 2004.

[29] – F.J. Herraiz-Martinez, V. Gonzalez-Posadas, L.E. Garcia-Munoz, D. Segovia-Vargas. "Multifrequency and dual-mode patch antennas partially filled with left-handed structures." *IEEE Trans. Ant. and Prop*. vol. 56, no. 8, pp. 2527-2539, 2008.

[30] – D.R. Smith, S. Schultz, P. Markos, C.M. Soukoulis. "Determination of effective permittivity and permeability of metamaterials from reflection and transmission coefficients." *Phys. Rev. B* vol. 65, pp. 195104 1-5, 2002.

[31] – X. Chen, T.M. Grzegorczyk, B-I Wu, J. Pacheco, J.A. Kong. "Robust method to retrieve the constitutive effective parameters of metamaterials." *Phys. Rev. E* vol. 70, pp. 016608 1-7, 2004.

[32] – D.R. Smith, D.C. Vier, Th. Koschny, C.M. Soukoulis. "Electromagnetic parameter retrieval from inhomogeneous metamaterials." *Phys. Rev. E* vol. 71, pp. 036617 1-11, 2005.

[33] – T. Koschny, P. Markos, D.R. Smith, C.M. Soukoulis. "Resonant and antiresonant frequency dependence of the effective parameters of metamaterials." *Phys. Rev. E* vol. 68, pp. 065602 1-4, 2003.

[34] – Y. Yuan, C. Bingham, T. Tyler, S. Palit, T.H. Hand, W.J. Padilla, D.R. Smith, N.M. Jokerst, S.A. Cummer. "Dual-band planar electric metamaterial in the terahertz regime." *Optics Express* vol. 16, no. 13, pp. 9746-9752, 2008.

[35] – T.H. Hand, J. Gollub, S. Sajuyigbe, D.R. Smith, S.A. Cummer. "Characterization of complementary electric field coupled resonant surfaces." *Appl. Phys. Lett*. vol. 93, pp. 212504 1-3, 2008.

[36] – O. Paul, C. Imhof, B. Reinhard, R. Zengerle, R. Beigang. "Negative index bulk metamaterial at terahertz frequencies." *Optics Express* vol. 16, no. 9, pp. 6736-6744, 2008.

[37] – DuPont Microcircuit Materials. *951 Green Tape Thick Film Composition*. Data sheet available from DuPont, 2001.

[38] – L. Li, D.H. Werner, J.A. Bossard, T.S. Mayer. "A model-based parameter estimation technique for wide-band interpolation of periodic moment method impedance matrices with application to genetic algorithm optimization of frequency selective surfaces." *IEEE Trans. Ant. and Prop*. vol. 54, no. 3, pp. 908-924, 2006.

[39] – R.S. Kshetrimayum, L. Zhu. "Guided-wave characteristics of waveguide based periodic structures loaded with various FSS strip layers." *IEEE Trans. Ant. and Prop*. vol. 53, no. 1, pp. 120-124, 2005.

Appendix A: Simple One-Dimensional FDTD MATLAB Code

```
% This simulates a Gaussian pulse, originating at the center of the grid,
% impinging on a dielectric from z=150 to 180.
% ABCs are included on both sides.

KE = 201;           % Range of z-domain (number cells)
kc = fix(KE/2);     % Center of z-domain (for pulse)
ex = zeros(1,KE);   % initialize Ex field
hy = zeros(1,KE);   % initialize Hy field
cb = zeros(1,KE);

% Initializations for the ABC on both sides
exlow1 = 0;
exlow2 = 0;
exhigh1 = 0;
exhigh2 = 0;

% Parameters for dielectric interface, where eps_start is the location
% of the interface and epsilon is the relative permittivity on the
% dielectric side of the interface
eps_start = 150;
epsilon = 4;

% Constant for E-field, including info about permittivity
% This constant is .5 in free space and .5 divided by relative permittivity
```

```
% in a dielectric material
cb(1,:) = 0.5;
cb(1,eps_start:eps_start+30) = .5/epsilon;

% These are parameters for use in the E-source, a Gaussian pulse
t0 = 36.0 ;         % Location in time of the pulse
spread = 12 ;       % Width of the pulse

% Number of time steps in the simulation
NSTEPS = 400 ;

for n=1:NSTEPS
    for k=2:KE
        ex(1,k) = ex(1,k) + cb(1,k).*(hy(1,k-1) -hy(1,k));
    end

    % This is the Gaussian pulse, added at the center of the grid
    pulse = exp(-0.5*((t0-n)/spread)^2.0);
    % The pulse is a soft source
    ex(1,kc) = ex(1,kc) + pulse;

    % The ABC at the left side
    ex(1,1) = exlow2;
    exlow2 = exlow1;
    exlow1 = ex(1,2);

    % The ABC at the right side
    ex(1,KE-1) = exhigh2;
    exhigh2 = exhigh1;
    exhigh1 = ex(1,KE-2);
```

```
    for k=1:KE-1
        hy(1,k) = hy(1,k) + 0.5*(ex(1,k) -ex(1,k+1)) ;
    end

    subplot(2,1,1),plot(ex);
    axis([0 200 -2 2]);
    xlabel('Problem space - Z-axis')
    ylabel('E-field intensity')
    title('Ex Field Intensity')
    subplot(2,1,2),plot(hy);
    axis([0 200 -2 2]);
    xlabel('Problem space - Z-axis')
    ylabel('H-field intensity')
    title('Hy Field Intensity')
    pause(0.03);
end
```

Appendix B: One-Dimensional Negative Index FDTD MATLAB Code

```
% This is a reimplementation of the 1D FDTD scheme similar
% to that of Ziolkowski & Heyman.  Uses a soft sinusoidal source
% at z=500 implemented in Ex.  This is at the resonant frequency that
% results in impedance being matched to free space, so reflections are
% minimized at material interfaces.

% Uses electric and magnetic current densities to calculate field strengths

% Output includes animation of Ex and Hy field propagation along problem
% space as well as instantaneous Poynting vector along z, with
% time-averaging of Poynting vector at 44000 time steps

% Code written by Alex Katko as part of ECE H783, towards
% completion of a senior honors thesis at the Ohio State University

clc

% Size of computational domain (1D)
KE = 5000;

% Field/current density initializations
Ex = zeros(1,KE);
Hy = zeros(1,KE);
Ky = zeros(1,KE);
Jx = zeros(1,KE);
Sz = zeros(1,KE);
Pz = zeros(1,KE);

Ptot = zeros(1,KE);

% Initialization of material parameters of interest
Gamma = zeros(1,KE);
wp = zeros(1,KE);

% Parameters of the problem: exact Courant condition satisfied here
f0=30e9;
w0 = f0*2*pi;
lambda = 3e8/f0;
dz = lambda/300;
dt = dz/(3e8);
wp(1,2000:3000) = 2.665e11;
Gamma(1,2000:3000) = 1e8;
gamma = 1e8;
```

```
w_p = 2.665e11;

% Constants
u0 = (4*3.1415926535897)*10^-7;
e0 = 8.854e-12;
T = 0;

% ABC Initializations
Exh1 = 0;
Exl1 = 0;

magorder = floor(log10(dz));

% Number of time steps for problem - 5000-10000 are needed for steady state
NSTEPS = 45000;

% Calculation of some parameters of interest
% Here permeability/permittivity using lossy Drude material
e=e0*(1-(w_p)^2/(w0*(w0+j*gamma)));
u=u0*(1-(w_p)^2/(w0*(w0+j*gamma)));

% Here relative permeability/permittivity using above
er=e/e0;
ur=u/u0;

% Here refractive index and wavenumber k (beta)
N = zeros(1,KE);
N(1,:) = 1;
N(2000:3000) = -1*sqrt(er*ur);
k_vector = w0*sqrt(e*u);

beta = zeros(1,KE);
beta(1,:) = w0*sqrt(e0*u0);
beta(1,2000:3000) = -1*w0*sqrt(e*u);

% Here impedance of material
Z = zeros(1,KE);
Z(1,:) = sqrt(u0/e0);
Z(1,2000:3000) = sqrt(u/e);
Impedance=sqrt(u/e);

e
u
k_vector
Impedance

for k=1:KE
        Sz(1,k) = (.5)^2*real(1/conj(Z(1,k)))*exp(-2*imag(beta(1,k))*k*dz)/2;
end

subplot(2,1,1),plot(real(N))
xlabel('Problem space, z')
ylabel('Refractive index n')
subplot(2,1,2),plot(real(Z))
```

```
xlabel('Problem space, z')
ylabel('Impedance Z')

pause

for n=1:NSTEPS

    % Time used for source
    T = T + 1;

    % Sinusoidal source calculation
    pulse = sin(w0*dt*T);

    % Magnetic field intensity calculation
    for k=1:KE-1
        Hy(1,k) = Hy(1,k) - (dt/(u0*dz)).*(Ex(1,k+1) - Ex(1,k) +
Ky(1,k).*dz);
    end

    % Magnetic current density calculation
    for k=1:KE-1
        Ky(1,k) = ((1-.5*dt.*Gamma(1,k))/(1+.5*dt.*Gamma(1,k))).*Ky(1,k) +
...
            ((u0*dt.*wp(1,k).^2)/(1+.5*dt.*Gamma(1,k))).*Hy(1,k);
    end

    % Electric field intensity calculation
    for k=2:KE
        Ex(1,k) = Ex(1,k) - (dt/(e0*dz)).*(Hy(1,k) - Hy(1,k-1) + ...
            .5*dz.*(Jx(1,k) + Jx(1,k-1)));
        Pz(1,k) = Ex(1,k)*Hy(1,k);
    end

    % Used for computing time-averaged Poynting vector when problem is
    % approximately steady-state
    if n>=44000 && n<44901
        Ptot = Ptot + Pz;
    end

    for k=1:KE
        Sz(1,k) = (.5)^2*real(1/conj(Z(1,k)))*exp(-2*imag(beta(1,k))*k*dz)/2;
    end

    % 1D ABCs implemented in electric field
    Ex(1,1) = Exl1;
    Exl1 = Ex(1,2);

    Ex(1,KE) = Exh1;
    Exh1 = Ex(1,KE-1);

    % Electric current density calculation
    for k=1:KE-1
        Jx(1,k) = ((1-.5*dt.*Gamma(1,k))/(1+.5*dt.*Gamma(1,k))).*Jx(1,k) +
...
```

```
            ((e0*dt.*wp(1,k).^2)/(2*(1+.5*dt.*Gamma(1,k)))).*(Ex(1,k+1) +
Ex(1,k));
    end

    % Addition of the source, as a soft E field source
    Ex(1,500) = Ex(1,500) + pulse;

    % Mod statement is included to speed up plotting, since domain is large
    if mod(n,5) == 0
    subplot(3,1,1),plot(Ex);
    axis([0 5000 -1 1]);
    text(5002,.75,sprintf('Step %d of\n%d',n,NSTEPS))
    xlabel(['Problem space, in m^',num2str(magorder)])
    ylabel('Ex field intensity')

    subplot(3,1,2),plot(Hy);
    axis([0 5000 -1/377 1/377]);
    xlabel(['Problem space, in m^',num2str(magorder)])
    ylabel('Hy field intensity')

    subplot(3,1,3),plot(Pz);
    xlabel('Problem space')
    ylabel('Poynting vector in z-hat')

    pause(.001);
    end

end

% Time averaging of Poynting vector
Pavg = Ptot./900;

figure(2)
plot(Pavg)
title('Time-average Poynting vector (z-hat)')
xlabel('Problem space')
ylabel('S(z-hat)')
```

Appendix C: Sample Retrieval Code Implemented in MATLAB

```
% Sets intermediate parameters from S matrix generated by HFSS simulations
for i=1:length(f)
    S11(i,1)=real(S(i,1))-j*imag(S(i,1));
    S21(i,1)=real(S(i,2))-j*imag(S(i,2));
    k0(i,1)=2*pi*f(1,i)/3e8;
end

% Plots magnitudes of S parameters for structure
figure(1)
plot(f0,abs(S11))
hold on
grid on
plot(f0,abs(S21),'r-.')
title('S parameter of Metamaterial')
xlabel('Frequency [GHz]')
ylabel('S parameters')
legend('S_1_1','S_2_1')
hold off

% Plots phases of S parameters for structure
figure(2)
plot(f0,angle(S11))
hold on
grid on
plot(f0,angle(S21),'r-.')
title('S Phase of Metamaterial')
xlabel('Frequency [GHz]')
ylabel('Phase of S parameters')
legend('S_1_1','S_2_1')
hold off

% Implementation of impedance retrieval, using passivity requirement to
% determine sign choice
for i=1:length(f)
    z(i,1)=sqrt(((1+S11(i,1))^2-(S21(i,1))^2)/((1-S11(i,1))^2-(S21(i,1))^2));
    if real(z(i,1))<0
        z(i,1)=-1*z(i,1);
    end
end

% Plot of real and imaginary parts of impedance
figure(3)
plot(f0,real(z))
hold on
```

```
grid on
plot(f0,imag(z),'-.')
title('Metamaterial Impedance')
xlabel('Frequency [GHz]')
ylabel('Impedance [\Omega]')
legend('Real Z','Imag Z')
axis([0 20 -2 2])
hold off

% Exponential term calculation...
for i=1:length(f)
    ex(i,1)=(S21(i,1))/(1-(S11(i,1))*(z(i,1)-1)/(z(i,1)+1));
end

%...followed by calculation of index. Note calculation of branches
for i=1:length(f)
    ni(i,1)=(real(log(ex(i,1))))/k0(i,1)/d;
    for k=1:5
        n0(i,k)=(imag(log(ex(i,1)))+2*pi*(k-3))/k0(i,1)/d;
        n(i,k)=n0(i,k)-j*ni(i,1);
    end
end

% Plot of true index branch
figure(4)
plot(f0,imag(n),'r-.')
hold on
grid on
plot(f0,real(n(:,3)))
title('Metamaterial Refractive Index')
xlabel('Frequency [GHz]')
ylabel('Refractive index')
legend('Imag n','Real n')
axis([0 20 -6 10])
hold off

% Calculation of permittivity and permeability using true index branch
for i=1:length(f)
    eps(i,1)=n(i,3)/z(i,1);
    mu(i,1)=n(i,3)*z(i,1);
end

figure(5)
plot(f0,real(mu))
hold on
grid on
plot(f0,imag(mu),'r-.')
title('Metamaterial \mu')
xlabel('Frequency [GHz]')
ylabel('Permeabiliy \mu')
legend('Real \mu','Imag \mu')
axis([0 20 -10 15])
hold off

figure(6)
plot(f0,real(eps))
```

```
hold on
grid on
plot(f0,imag(eps),'r-.')
title('Metamaterial \epsilon')
xlabel('Frequency [GHz]')
ylabel('Permeabiliy \epsilon')
legend('Real \epsilon','Imag \epsilon')
axis([0 20 -20 2])
hold off
```